Article

Cell Reports

Systems-Genetics-Based Inference of a Core Regulatory Network Underlying White Fat Browning

Graphical Abstract

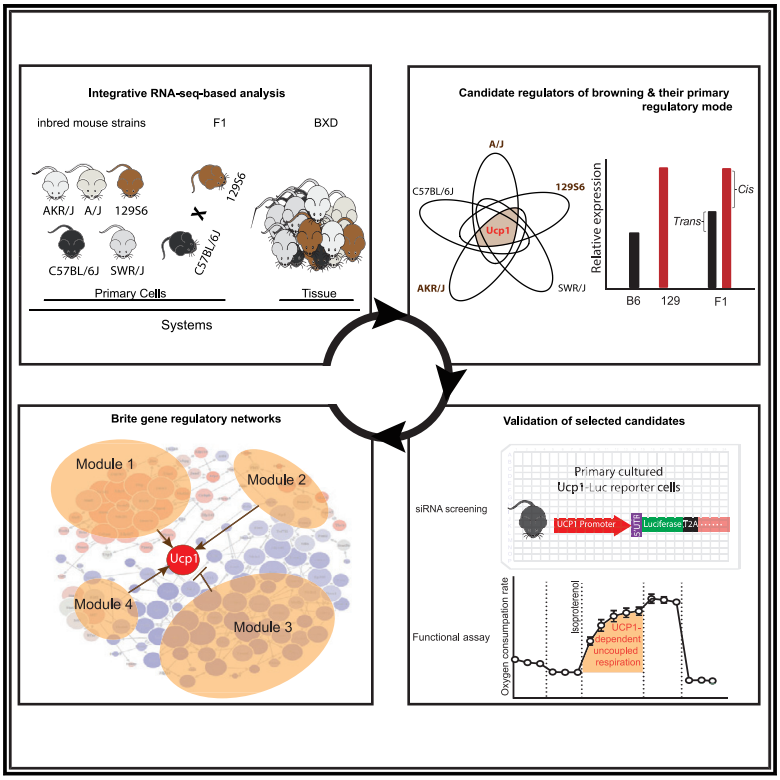

Authors

Yongguo Li, Petra C. Schwalie, Andrea Bast-Habersbrunner, ..., Tobias Fromme, Bart Deplancke, Martin Klingenspor

Correspondence

bart.deplancke@epfl.ch (B.D.), mk@tum.de (M.K.)

In Brief

Browning of white fat, which turns an energy-storing organ into an energy-dissipating one, holds promise for the development of novel therapeutics against obesity. By exploiting intrinsic mouse strain variation and applying a systems-genetics approach, Li et al. reveal a comprehensive gene regulatory network that controls this browning process.

Highlights

- The browning capacity of white adipose tissue is under complex genetic control
- Genetic architecture of brite adipogenesis is built from several genetic models
- Dozens of Ucp1 regulating factors are validated
- A core browning regulatory network with four distinct regulatory modules is revealed

Li et al., 2019, Cell Reports *29*, 4099–4113
December 17, 2019
https://doi.org/10.1016/j.celrep.2019.11.053

CellPress

Cell Reports
Article

Systems-Genetics-Based Inference of a Core Regulatory Network Underlying White Fat Browning

Yongguo Li,[1,2,4] Petra C. Schwalie,[3,4] Andrea Bast-Habersbrunner,[1,2] Sabine Mocek,[1,2] Julie Russeil,[3] Tobias Fromme,[1,2] Bart Deplancke,[3,*] and Martin Klingenspor[1,2,5,*]

[1]Chair for Molecular Nutritional Medicine, TUM School of Life Sciences Weihenstephan, Technical University of Munich, Gregor-Mendel-Str. 2, 85354 Freising, Germany

[2]EKFZ-Else Kröner-Fresenius Center for Nutritional Medicine, Technical University of Munich, Gregor-Mendel-Str. 2, 85354 Freising, Germany

[3]Institute of Bio-engineering, School of Life Sciences, EPFL and Swiss Institute of Bioinformatics, 1015 Lausanne, Switzerland

[4]These authors contributed equally

[5]Lead Contact

*Correspondence: bart.deplancke@epfl.ch (B.D.), mk@tum.de (M.K.)

https://doi.org/10.1016/j.celrep.2019.11.053

SUMMARY

Recruitment of brite/beige cells, known as browning of white adipose tissue (WAT), is an efficient way to turn an energy-storing organ into an energy-dissipating one and may therefore be of therapeutic value in combating obesity. However, a comprehensive understanding of the regulatory mechanisms mediating WAT browning is still lacking. Here, we exploit the large natural variation in WAT browning propensity between inbred mouse strains to gain an inclusive view of the core regulatory network coordinating this cellular process. Combining comparative transcriptomics, perturbation-based validations, and gene network analyses, we present a comprehensive gene regulatory network of inguinal WAT browning, revealing up to four distinct regulatory modules with key roles for uncovered transcriptional factors, while also providing deep insights into the genetic architecture of brite adipogenesis. The presented findings therefore greatly increase our understanding of the molecular drivers mediating the intriguing cellular heterogeneity and plasticity of adipose tissue.

INTRODUCTION

Obesity develops when energy intake chronically exceeds energy expenditure. The increased prevalence of obesity and its associated metabolic disorders present a major public health challenge around the world (Ng et al., 2014). Current therapeutic strategies for correcting the obesity-causing energy imbalance involve either decreasing energy uptake or increasing energy expenditure. The discovery of active brown adipose tissue (BAT) in adult humans opens new avenues to increase energy expenditure, because the major function of BAT is to dissipate energy as heat (thermogenesis) via uncoupling protein1 (UCP1)-mediated leak respiration (Betz and Enerback, 2017; Tseng et al., 2010). Moreover, beyond boosting energy expenditure, we recently demonstrated that BAT thermogenesis is involved in control of satiation that might also be applicable to further promote negative energy balance (Li et al., 2018). Strenuous efforts are now undertaken to learn how to expand or activate BAT in ways that might be therapeutic in humans (Scheele and Nielsen, 2017; Sidossis and Kajimura, 2015). Beyond brown adipocytes, a new type of thermogenic adipocytes, known as brite (brown-in-white) or beige adipocytes, was identified. These brite cells develop predominantly in white adipose tissue (WAT) and exist in both rodents and humans (Harms and Seale, 2013; Li et al., 2013). Increasing the relative abundance of brite cells in WAT offers an opportunity to both highly increase the mass of thermogenic brite adipose tissues that are accessible for therapeutic activation and to decrease the amount of WAT, thereby turning an energy-storing organ into an energy-dissipating one.

Brite cells can be found most readily in subcutaneous inguinal adipose tissue, but are rather scarce in epididymal/perigonadal adipose tissue (Kozak and Koza, 2010; Li et al., 2014a). The propensity to accumulate brite cells is also modulated by genetic factors, as illustrated by variation among inbred mouse strains (Kozak and Koza, 2010). Mice of some strains, such as C57BL/6J, are highly resistant to the induction of brite adipocytes by adrenergic stimulation, whereas others, such as A/J and 129, are very sensitive, with levels of UCP1 in retroperitoneal fat approaching that of interscapular BAT (Guerra et al., 1998). In support of a physiological role for brite adipocytes in energy balance, murine-strain-dependent differences in resistance to diet-induced obesity have been attributed to the inducibility of brite adipocyte recruitment in WAT and muscle (Almind et al., 2007; Watson et al., 2000). Sympathetic fibers in the parenchym of adipose tissues show an increased density during cold acclimation, which positively correlates with the number of brite adipocytes in mice of the B6 and 129 strains. This suggests that strain differences in the sympathetic tone may be one of the principal causes for the different browning propensity between strains (Vitali et al., 2012). However, we found that, beyond systemic cues such as innervation and hormone levels, mouse strain differences in brite adipogenesis are sustained in cultured primary adipocytes, a condition where extrinsic cues can be largely excluded

(Li et al., 2014a). Furthermore, adipogenic progenitor abundance analyses did not reveal any strain differences so far (Li et al., 2014a; Schulz et al., 2011), indicating that cell intrinsic genetic differences in browning propensity may be the principal causes for the different browning propensity between strains.

A number of genes, including transcription factors (TFs) and metabolism-related genes, have been linked to brite adipogenesis through studies with genetically modified mice or single gene studies (reviewed in Harms and Seale, 2013; Kozak and Koza, 2010; Pradhan et al., 2017b). However, a comprehensive understanding of the regulatory mechanisms mediating WAT browning is still lacking. To address this, we decided to build on initial efforts by Koza et al. (2000) and Xue et al. (2005) and exploit the variation in browning propensity among mouse strains (Guerra et al., 1998) as a natural filter of molecular noise, thus enabling us to zoom in on the core regulators of the browning program across different genotypes. Specifically, we used an RNA sequencing (RNA-seq)-based comparative transcriptomic approach to molecularly characterize three such genetic systems showing variation in ingWAT browning: *in vitro* brite adipogenesis across (1) five inbred mouse strains—C57BL/6J (BL6/J), 129S6sv/ev (129S6), A/J, AKR/J, and SWR/J—with distinct WAT browning propensities as well as (2) F1 hybrids from a cross between a high (129S6) and a low (BL6/J) browning strain, and (3) *in vivo* WAT and BAT of the BXD genetic reference panel, consisting of >40 recombinant inbred, phenotyped mouse strains (Andreux et al., 2012). Comparative transcriptomic analyses of inguinal stromal vascular fraction (ingSVF) cells before and after *in vitro* brite differentiation revealed thousands of differentially expressed genes showing positive and negative correlation with browning, as measured by *Ucp1* induction. A subset of the highly *Ucp1*-correlated transcription (co-)factors, adipokines, metabolic enzymes, and long noncoding RNAs, with no previous link to WAT browning, were also highly correlated to *Ucp1* expression *in vivo* across BXD mice. Through allele-specific expression analyses of F1 hybrids, we uncovered system-specific imprinting as well as the primary genetic regulatory mode (*cis*-, *trans*-, or *cis* × *trans*) for hundreds of genes during browning. Using an *Ucp1*-reporter system, we validated the role of 25 regulators such as the TFs FHL1, MXD1, and ZFP521 through knockdown experiments in ingSVF. Combining our data, we present a comprehensive gene regulatory network of ingWAT browning, revealing up to four distinct regulatory modules with key roles for uncovered TFs, and also provide deep insights into the genetic architecture of brite adipogenesis. Together, our multilayered study greatly increases our understanding of the regulatory mechanisms underlying cellular heterogeneity and plasticity of adipose tissue.

RESULTS

The Browning Capacity of White Adipose Tissue Is under Genetic Control

To gain an overview of strain variation in browning capacity, we first performed a transcriptomic analysis of cell cultures from inguinal WAT across mouse strains, because, as noted above, many cell-extrinsic cues such as sympathetic innervation, angiogenesis, and hormone levels could otherwise influence *Ucp1* expression (Figure 1A). Beyond this advantage, we can also better separate the differentiated from undifferentiated states. To explore the *in vivo* relevance of identified regulators based on this *in vitro* system, we also considered gene expression profiles from inguinal WAT derived from BXD strains under both chow (CD) and high fat (HFD) diets (Andreux et al., 2012; Wu et al., 2014) (Figure 1A).

Our transcriptomic profiling revealed pronounced differences in browning propensity among mouse strains both in primary cultures (Figures 1B–1D, S1A, and S1B) and *in vivo* (Figures 1E, 1F, S1C, and S1D). Importantly, these differences were specific to browning (as also confirmed by brown marker gene expression) (Figures 1C, 1D, and S1B; Table S1), because no difference was observed in adipogenesis per se, given that adipogenic markers such as *Pparg*, *Adipoq*, and *Fapb4* showed comparable induction levels across all strains (Figure 1D; Table S1). In primary cultures, cells of the SWR/J genetic background resisted browning as also revealed by lowest *Ucp1* expression compared to other strains (Figures 1B and S1A), despite the well-established diet-induced obesity (DIO)-resistant metabolic phenotype of SWR/J mice (Kless et al., 2017; West et al., 1994). In contrast, cells of the obesity-prone AKR/J genetic background displayed a comparable browning capacity to those of the obesity-resistant A/J and 129S6 strains, demonstrating that the *in vitro* browning capacity is not always coupled with the DIO propensity. Finally, we observed that *Ucp1* expression in the BL6/J genetic background is higher than SWR/J but lower than that in A/J, AKR/J, and 129S6 (Figure 1B).

As expected, we found *Ucp1* expression to be higher in BAT compared to ingWAT among the BXD strains (Figures 1E, 1F, and S1C–S1E). Interestingly, *Ucp1* showed significantly higher expression variability (p value $<10^{-6}$ Flinger-Kileen's test) among the BXD strains in ingWAT compared to BAT. Moreover, HFD feeding appeared to increase *Ucp1* expression in most of the BXD strains, while levels remained correlated with the initial *Ucp1* expression (Figure 1F). To explore the physiological relevance of this variation in *Ucp1* expression, we looked for annotated phenotypes that were correlated to *Ucp1* expression levels ($p \leq 0.1$, $|rho| \geq 0.4$). Most of these phenotypes showed a positive correlation with *Ucp1*, and most associations were present under CD (Figure 1G). For instance, we found that the change in body temperature in response to cold exposure for 1 h at 4°C was highly correlated to *Ucp1* levels in both ingWAT and BAT (Figures 1H and S1F). Overall, when considering the top five associations in any of the three datasets, we found positive correlations with phenotypes related to respiration and body temperature upon cold exposure, which were absent among negative correlations (Figure S1F). Thus, the observed strain variation in browning propensity is associated with variation in physiological properties that have been previously connected to browning. These results validate the relevance of the employed genetic model and indicate that variant alleles for genes associated with *Ucp1* expression and the brite adipogenesis program are extant within these inbred strains.

Together, we conclude that our *in vitro* and *in vivo* models provide complementary genetic systems that can be employed to identify genes that are critical for the induction of the browning program in progenitor cells represented in the SVF of ingWAT.

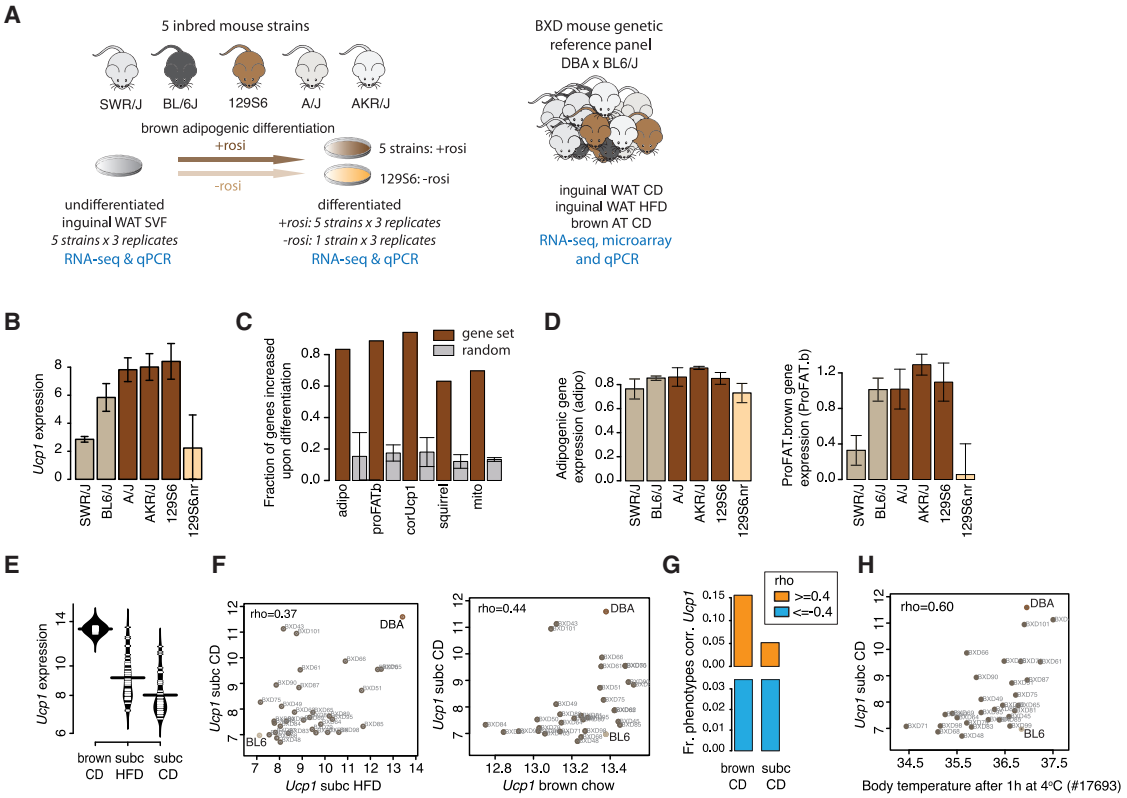

Figure 1. The Inguinal Fat Browning Capacity Is under Genetic Control

(A) Schematic overview of employed genetic models to study the molecular basis of brite adipogenesis: *in vitro* brown adipogenesis of primary inguinal cell cultures from five inbred mouse strains (left) and brown and inguinal (subc) fat depots derived from the mouse BXD genetic reference panel under chow diet (CD) and high fat diet (HFD). Rosi, rosiglitazone.

(B) RNA-seq-based *Ucp1* expression levels upon brite adipocyte differentiation in five distinct mouse strains as well as a no rosiglitazone (nr) control (n = 3).

(C) Differentiation increases expression levels of gene sets previously functionally connected to brown adipogenesis: general adipogenic markers (adipo), genes highly correlated to *Ucp1* in the BIOGPS database (Ucp1corr), genes part of a recently determined mature brown fat signature (proFAT.b) (Cheng et al., 2018), BAT-specific genes showing seasonal expression in ground squirrels (Hampton et al., 2013), and genes involved in mitochondrial function (mito) (Table S1; STAR Methods).

(D) Expression of adipogenic and mature brown fat specific (proFAT.b) genes among primary cultures derived from five distinct mouse strains. nr, no rosiglitazone control (n = 3).

(E) *Ucp1* expression across BXD strains in brown and subcutaneous (subc) fat under control diet (CD) and high fat diet (HFD) (only for subc) (n = 33).

(F) Relation between *Ucp1* expression levels in inguinal (subc) and brown fat under chow (CD) and high fat diet (HFD) (n = 33).

(G) The fraction (Fr.) of previously measured phenotypes (Andreux et al., 2012) positively (orange) and negatively (blue) correlated (rho $\geq$0.4 or $-$0.4, respectively) with *Ucp1* expression in brown and inguinal (subc) fat under chow diet (CD) across BXD mice.

(H) Correlation between the *Ucp1* expression level in inguinal fat and whole-body temperature after 1 h cold exposure at 4°C across BXD mice (n = 33).

Error bars represent mean ± SD.

See also Figure S1 and Table S1.

Extensive Transcriptomic Changes Arise upon Brite Adipogenesis across Mouse Strains, Revealing Candidate Regulators

To systemically identify genes involved in browning of inguinal SVF, we first asked which gene transcripts are regulated upon adipogenesis across cultures from the five inbred mouse strains (STAR Methods). For each strain, we detected extensive differences, with a total of over 4,000 genes showing significant changes, approximately half of these being shared across all strains (Figures 2A and S2A; Table S2). Among strains, the number of induced genes correlated with the extent of browning. For instance, the two strains showing the highest increase in the expression of brown (*Ucp1* and ProFAT.b signature) (Cheng et al., 2018) (Table S1) and brite adipocyte marker genes (AKR/J and 129S6) (Figures 1B and 1D) also showed the largest number of significantly differentially expressed genes (Figure S2A). More differences between the strains appeared after differentiation, with the strain that had the least browning potential (SWR/J) becoming most transcriptionally distinct only upon brite adipogenesis (Figures S2B and S2C). The expression differences were largely in extent rather than in kind, corresponding to lower fold-changes (FCs) (Figure 2B). Interestingly, the lowest browning strain was transcriptionally most similar to the non-rosiglitazone treated control samples after differentiation (Figures 2B and S2B). This suggests that *in vitro*, these cells may lack

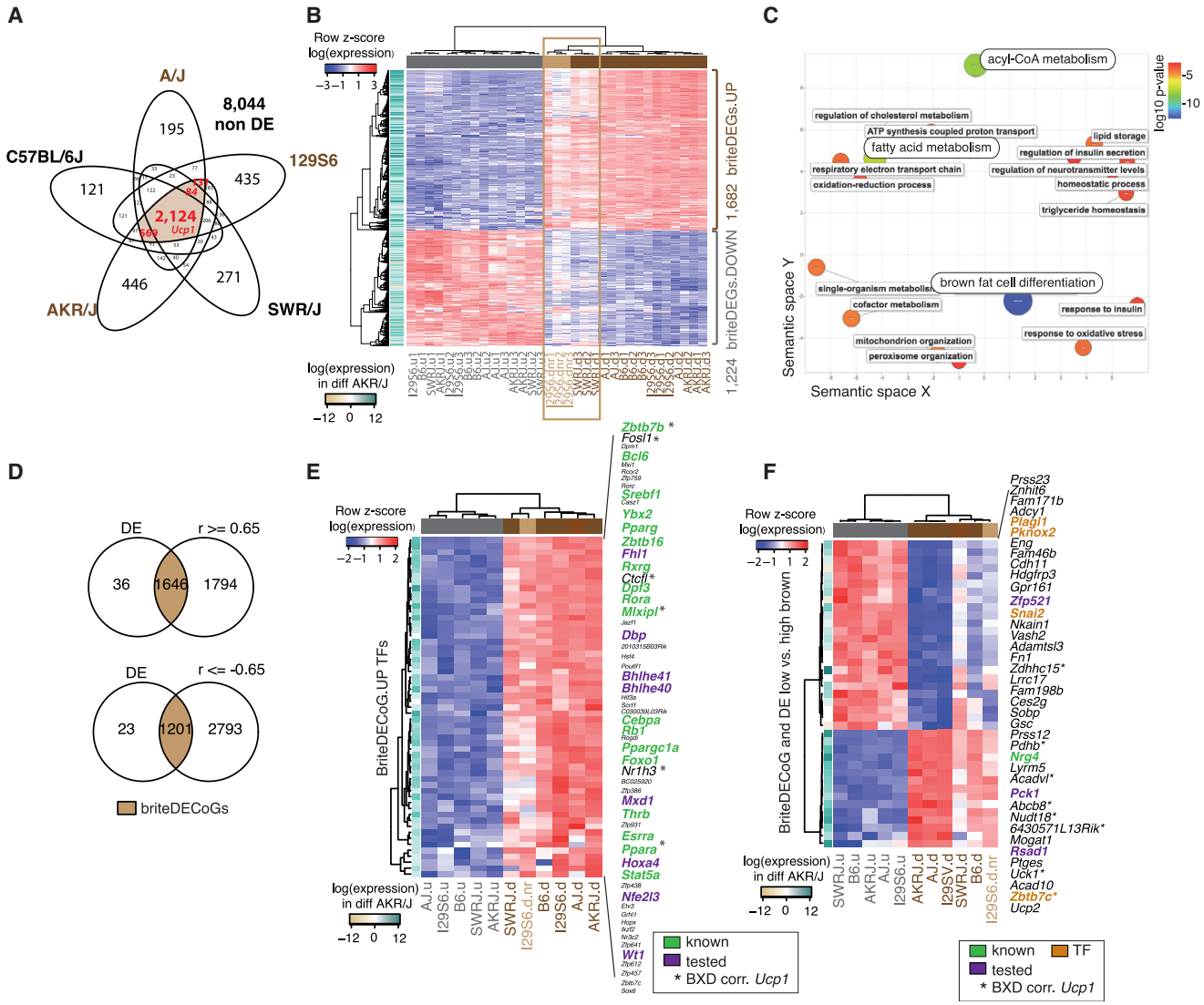

Figure 2. Extensive Transcriptomic Changes upon Browning of Inguinal SVF Cells

(A) Venn diagram showing the overlap of genes that are significantly differentially expressed upon brite adipogenesis in the five inbred mouse strains.

(B) Heatmap showing expression of "brite differentially expressed genes" (briteDEGs) before and after brown adipogenesis. Included genes are only commonly deregulated across the three strains with high browning propensity (A/J, AKR/J, and 129S6).

(C) REViGO semantic analysis of GO biological processes enriched in the 1,682 upregulated briteDEGs.

(D) Overlap between briteDEGs and genes correlating with *Ucp1* (absolute value of Pearson's rho ≥ 0.65, $p < 0.01$) across all five strains. The shared fraction is referred to as briteDECoGs.

(E) Heatmap of the TFs potentially playing positive regulatory roles during inguinal WAT browning. All upregulated briteDECoGs are included. Green, genes previously involved in browning or core adipogenic regulation. Purple, genes tested here for a role in *Ucp1* regulation. *Genes significantly correlating with *Ucp1 in vivo* across BXD mice.

(F) Heatmap of briteDECoGs that are also differentially expressed between mouse strains showing low (SWR/J and BL/6) versus high (A/J, AKR/J, 129S6) browning potential. Orange, genes encoding TFs. Green, genes previously involved in browning or core adipogenic regulation. Purple, genes tested here for a role in *Ucp1* regulation. *Genes significantly correlating with *Ucp1 in vivo* across BXD mice.

See also Figure S2 and Tables S2, S3, and S4.

the ability to respond to rosiglitazone and thus fail to sufficiently induce the brite transcriptional program.

As primary cultures derived from A/J, AKR/J, and 129S6 mice had high browning propensities (Figures 1B and 1D), we defined the genes significantly up- (1,682) or downregulated (1,224) upon brite adipocyte differentiation across these three mouse strains as "brite differentially expressed genes" (briteDEG) (Table S2). Gene Ontology (GO) enrichment analysis of the upregulated genes revealed a strong association with brown adipogenesis, mitochondria, respiration, and lipid metabolism (Figure 2C; Table S3). In contrast, downregulated genes were functionally associated to early development, differentiation, proliferation, and cell

division (Figure S2D; Table S3). These results are consistent with the notion that upon differentiation, SVF-derived cells lose their proliferative and multipotent abilities and specialize by turning on the brite adipocyte regulatory program, thereby computationally validating the briteDEG set.

To specifically identify genes involved in *Ucp1* regulation, we applied *Ucp1*-correlation analysis as a second strategy to further filter the briteDEGs. In total, we found that a large number of genes showed a significant correlation with *Ucp1* (>3,000 at Pearson's r $\geq$0.65; >2,000 at Pearson's r $\geq$0.80) (Figures 2D and S2E; Table S2). Of note, the vast majority of briteDEGs were also correlated with *Ucp1* (Figures 2D and S2E; Table S2). Among the differentially expressed genes correlating with *Ucp1* (briteDECoGs), there are (1) well established brown-specific marker genes such as *Cidea*, *Cox7a1*, *Ppargc1a*, *Cox8b*, and *Elovl3*; (2) the brown specific surface maker *Slc36a2* (Ussar et al., 2014); (3) the brown fat-enriched secreted factor *Nrg4* (Wang et al., 2014); (4) genes important for brown adipocyte function such as *Cd36* (Anderson et al., 2015; Bartelt et al., 2011), new lipase *Ced1d* (Yang et al., 2019), genes (*Slc25a44* and *Bckdha/b*) involved in branched-chain amino acids catabolism (Yoneshiro et al., 2019); as well as (5) established TFs such as Zinc finger and BTB domain containing 16 (*Zbtb16*) (Plaisier et al., 2012), myocardin-related transcription factor A (*Mkl1*) (McDonald et al., 2015), or the TF *Hoxa4*, recently implicated in brown adipogenesis (Pradhan et al., 2017a). A summary of such genes that have already been demonstrated to be of functional relevance to browning or brown fat function is presented in Table S4. Their identification indicates that the genetic systems, and thus our applied strategy, can efficiently reveal the molecular architecture of brite adipogenesis. Strikingly, we thereby found that all four transcription factors whose expression levels were recently reported to (anti)correlate with the pharmacologically induced browning of SVF cells based on single-cell RNA-seq measurements (Burl et al., 2018) are present in this *Ucp1* expression correlation gene list. Specifically, while *Pparg*, *Cebpa*, and *Srebf1* were, as expected, based on previous studies (Table S4) highly induced upon browning, the expression of *Hmgb2*, not previously implicated in *Ucp1* regulation, was strongly reduced. Moreover, we found that the fraction of genes showing significant correlation with *Ucp1* expression across BXD strains was 2–3 times higher among upregulated genes (briteDECoGs.UP) compared to downregulated genes (briteDECoGs.DOWN) or compared to genes not showing a significant change (Figure S2F). Many of the briteDECoGs.UP genes are thus likely linked to browning both *in vitro* and *in vivo*.

Globally, the identified candidate genes may function either as (1) transcriptional regulators of *Ucp1*, (2) essential functional components of brite adipocytes, or (3) specific markers of brite adipocytes. In total, we revealed 57 TFs (Figure 2E), 346 mitochondrial proteins, 20 surface markers, and 37 long non-coding RNAs (lncRNAs) that were positively associated with brite adipogenesis, and an even larger number of negative associations (Figure S1G; Table S2). Finally, we asked which of these genes also showed a significant difference between their expression in the two low browning strains (SWR/J and BL6/J) versus the three high browning ones (AKR/J, 129S6, and A/J), because such a comparison could reveal pathways that are deregulated when *Ucp1* fails to be fully induced (Figure 2F; STAR Methods). This analysis revealed only a small number (39) of such genes, including those encoding the TFs PLAGL1, ZFP521, PKNOX2, SNAI2, and ZBTB7C. We found that all of them, with the exception of ZBTB7C, are higher expressed in undifferentiated samples, raising the intriguing possibility that they are involved in *Ucp1* repression.

Together, our transcriptomic analyses map out the common and individual transcriptomic changes upon browning of inguinal WAT cells across mouse strains and provide a valuable resource for the identification and further characterization of novel regulators of browning.

F1 Hybrids Reveal System-Specific Imprinting and Primary Genetic Regulatory Modes

Mutations that affect the function of *cis*- and *trans*-regulatory factors contribute to phenotypic diversity (Deplancke et al., 2016). The F1 genetic cross analysis is very effective at disambiguating *cis*- and *trans*-acting regulation genome-wide (Goncalves et al., 2012; Shen et al., 2014; Wittkopp and Kalay, 2011). By placing two alleles in a shared *trans* environment, the relative *cis* and *trans* contributions to a measured molecular trait can be evaluated. Using this approach, we performed allele-specific RNA-seq analyses in primary cultures derived from BL6/Jx129S6 (resulting from BL6/J male x 129S6 female, initial) and 129S6xBL6/J (resulting from 129S6 male x BL6/J female, reciprocal) F1-intercrossed mice (Figure 3A).

We found that cells derived from the F1 hybrids have an intermediate browning capacity compared to that of the respective parental types, with no difference between the two mating designs, indicating there are no obvious parent-of-origin effects on browning capacity (Figure 3B). Global transcriptomic differences were the strongest between undifferentiated and differentiated samples, and BL6/J versus 129S6 gene expression separated clearly upon differentiation (Figure S3A). Of note, we found that 86% of the briteDEGs are also differentially expressed in the F1 cultures (briteDEG.F1s) (Tables S2 and S5), demonstrating that transcriptomic changes upon browning of inguinal SVF cells are highly consistent in inbred strains and F1 models (Figure 3C). Interestingly, six of these genes showed a parent-of-origin biased expression, including those encoding the TFs *PLAGL1* (also a briteDECoG) and *SOX6* (Figures 3D–3F; Table S6). A similar number of genes were detected as imprinted in undifferentiated and differentiated cells, several of which were previously known (Table S7) such as the above-mentioned TF *Plagl1* (Varrault et al., 2006) and the component of the small nuclear ribonucleoprotein complex *Snrpn* (Shemer et al., 1997) (another briteDECoG) (Figure S3B).

After removing all imprinted genes from our allele-specific analyses, we found that the primary regulatory mode in our genetic system is *cis*, followed by *trans* and finally *cis* and *trans* (Figures 3G, 3H and S3C; Table S6), in line with previous studies in other mouse tissues and strains (Goncalves et al., 2012; Shen et al., 2014; Wittkopp and Kalay, 2011). Interestingly, we observed an increase in the fraction of *cis*-regulated genes upon differentiation, consistent with larger transcriptomic differences between BL6/J and high browning strains such as 129S6 upon browning (Figures 3G, S2C, and S3C). We found 12 briteDECoGs regulated in *cis*

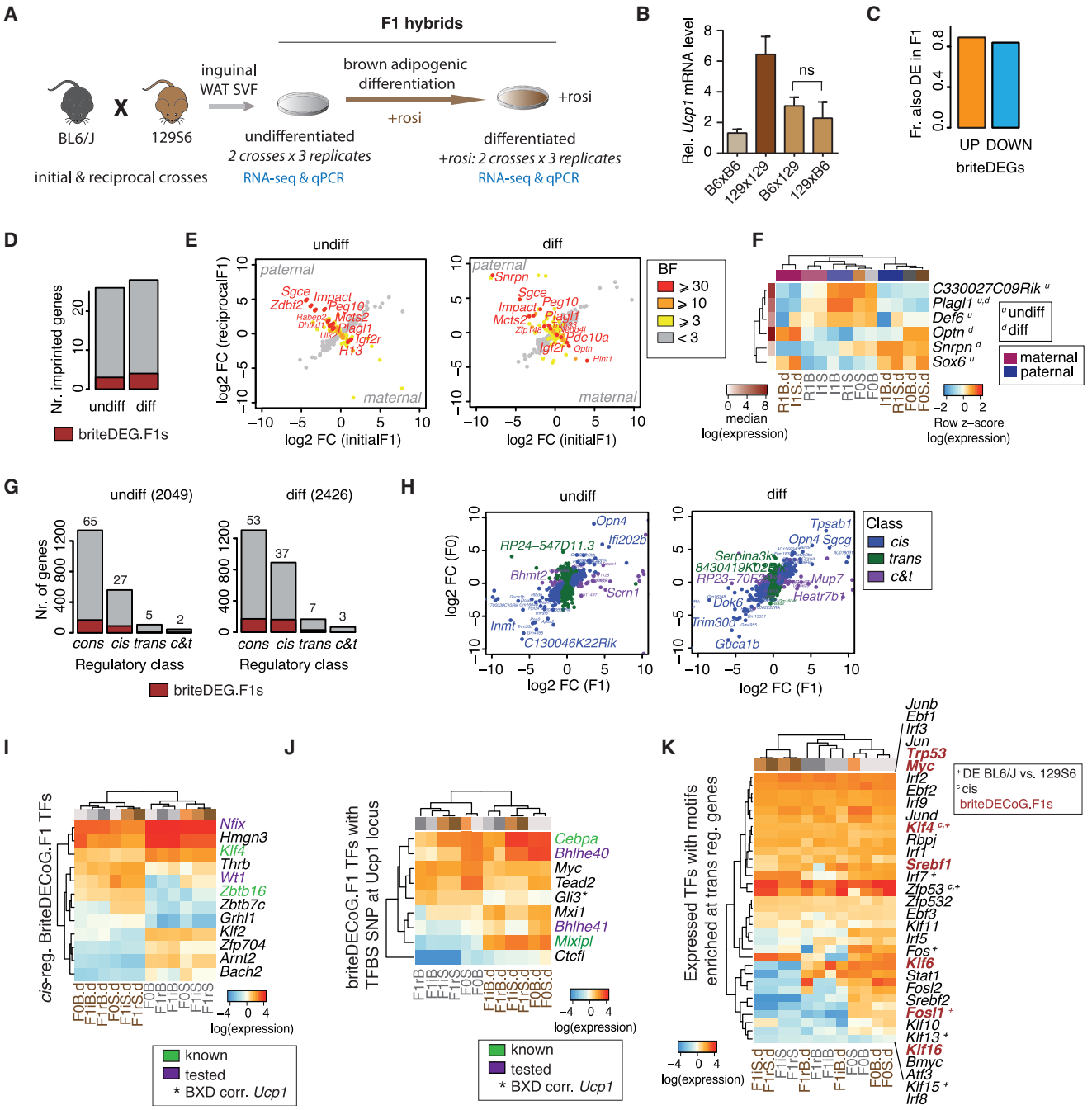

Figure 3. Allele-Specific RNA-Seq Analyses in F1 Hybrids

(A) Schematic depiction of the experimental set-up: the high browning strain 129S6 was crossed with the low browning strain BL6/J, both as an initial (129S6 female versus BL6/J male) and a reciprocal cross (129S6 male versus BL6/J female). Genome-wide RNA-seq expression was measured in SVF-derived cells after plating (undiff, day 3), as well as after brite adipogenesis (diff). Rosi, rosiglitazone.

(B) Expression of *Ucp1* in F1 hybrids and the parental lines (F0) after brite adipogenesis as measured by qPCR (N = 3, mean ± SD). ns,: non-significant differences, t test.

(C) Fraction of UP (orange) and DOWN (blue) briteDECoGs also significantly differentially expressed (false discovery rate [FDR] 0.01, |FC| > 2) in F1 hybrids.

(D) Number of genes imprinted in SVF-derived cells before and after brite adipogenesis. In red, number of genes that are also briteDECoGs.

(E) Log2 fold-change (FC) of gene expression in 129S6 versus BL6/J in initial versus reciprocal mice crosses before (undiff) and after (diff) brite adipogenesis. Imprinted genes are marked in yellow-orange-red, according to the Bayes factor (BF). Most likely imprinted genes (red) are highlighted.

(F) Row-normalized gene expression in the F1 hybrids and the parental lines (F0) of the imprinted genes found among briteDECoGs. Pink, maternal samples; blue, paternal samples; brown/gray, parental samples. Red-to-white, median gene expression across all samples. F0 B(S).d: BL6/J allele (129) in differentiated

(legend continued on next page)

(Figure 3I), including those encoding the known adipogenic regulators ZBTB16 and KLF4 (Park et al., 2017; Plaisier et al., 2012), but also the uncovered TF ZBTB7C, highlighted above as significantly different in low versus high browning strains, and also correlated with *Ucp1 in vivo* across BXD mice.

Notably, *Ucp1* also represented a case of *cis*-acting imbalance, favoring 129S6 alleles. We thus searched for SNPs at the *Ucp1* locus predicted to affect TF binding affinity and retained nine expressed TFs that could be responsible for the observed *cis* effect (Figure 3J; STAR Methods). This included the canonical adipogenic regulator CEBPA, the TF ChREB (encoded by *Mlxipl*), previously reported to be in control of *Ucp1* expression in response to glucose and T3 (Katz et al., 2018), the pluripotency and cell-cycle regulator MYC, but also TFs not previously linked to *Ucp1* regulation such as BHLHE40, BHLHE41, MXI1, and CTCFL.

Next, we focused on the large number of genes regulated in *trans*, exploring which TFs could control their differential expression. We asked which TF binding motifs were overrepresented at the promoters of *trans*-regulated genes (STAR Methods), and retained 33 such TFs that also showed expression in SVF cells (Figure 3K). Seven of these were also briteDECoG.F1s, among which, KLF4 stood out for also being regulated in *cis*. Moreover, a role of KLF4 in adipogenesis has been reported (Birsoy et al., 2008), although this TF has recently been found to be dispensable for brown adipocyte differentiation and development *in vivo* (Park et al., 2017), consistent with a lack of correlation with *Ucp1* across BXD mice (Figure S2G). As KLF4, most of the detected factors tended to be highly expressed in undifferentiated cells, pointing toward a possible repressive action on brown adipogenesis. In contrast, the EBF TF family, which also emerged from the motif overrepresentation analysis, was consistently expressed across differentiation, raising the possibility that a differential activity of the known regulator of brown adipogenesis, EBF2 (Rajakumari et al., 2013), could occur at the post-transcriptional level and drive some of the observed *trans* effects.

Together, our results suggest that a large extent of variation in browning propensity is driven by non-coding regulatory variation, because *cis* effects predominate in our genetic system. We also determined the primary regulatory mode of hundreds of genes with a genetic or parent-of-origin bias across brite adipogenesis, highlighting novel putative direct regulators of *Ucp1* expression and the broader brown fat gene regulatory program.

Novel Regulators of White Fat Cell Browning

To validate the roles of some of the identified candidate regulators of brite adipogenesis, we first performed a small interfering RNA functional screen. We employed primary cultured adipocytes derived from an Ucp1promoter-Luciferase-T2A-iRFP-T2A-UCP1 knock in mouse model, where the luciferase activity can reliably represent endogenous *Ucp1* expression both *in vivo* and *in vitro* (Wang et al., 2019) (Figure S4A). Due to the sensitivity and high-dynamic range of the luciferase activity, these cells provide a simple cost- and time-saving system for the screening of candidate genes and compounds that modulate *Ucp1* expression, even in a high throughput manner. As a primary screen, 28 DECoG.F1s candidates (Figures 4A–4C; STAR Methods) with various levels of *in vitro* and *in vivo* expression as well as correlation to *Ucp1* representing TFs, metabolic enzymes, and long noncoding RNAs were targeted using small interfering RNA-mediated knockdown (KD). Primary cultured inguinal adipocytes were reverse transfected after induction and differentiated for 3 days before the luciferase activity was determined. In total, we found that 15 candidates are positive regulators of *Ucp1*, because their KD led to a decrease of *Ucp1*-driven luciferase activity, while eight acted as negative regulators (Figure 4D). We note that this corresponds to 82% of the initial candidates being validated and 78% of the validated candidates showing an effect on *Ucp1* expression that goes in the predicted direction. This included six genes encoding TFs not previously associated with *Ucp1* regulation during brite adipogenesis—*Fhl1*, *Mxd1*, *Wt1*, *Bhlhe41*, *Hoxa4*, and *Dbp*.

To further validate this primary screen, we employed western blot and microplate-based respirometry in wild-type inguinal adipocytes transfected with small interfering RNAs (siRNAs) to check UCP1 protein levels and UCP1-mediated uncoupled respiration, respectively. Fully confirming the results of the siRNA screen, KD of *Mxd1*, *Fhl1*, *Steap4*, *Impa2*, and *Plin5* led to downregulation of the UCP1 protein and impaired UCP1-mediated uncoupled respiration upon isoproterenol stimulation, while KD of *Zfp521* had the reverse effect (Figures 4E–4G and S4B–S4D). Additionally, we targeted *Mxd1* and *Fhl1* with independent Dicer-substrate siRNAs (dsiRNAs). We found that UCP1 protein expression is substantially lower in the adipocytes depleted of *Mxd1* and *Fhl1* than in the control siRNA-transfected cells, while again, the reverse is true for *Zfp521* (Figure 4G). We noted that for none of the factors, differentiation and lipid accumulation is impaired (Figure S4D). These results suggest

adipocytes derived from F0; R1B(S).d: BL6/J allele (129) in differentiated adipocytes derived from a reciprocal (129S6 male versus BL6/J female) cross; I1B(S).d: BL6/J allele (129) allele in differentiated adipocytes derived from an initial (129S6 female versus BL6/J male) cross; Annotation without.d indicates undifferentiated SVFs.

(G) Number of genes with conserved (cons), *cis*, *trans*, or *cis* and *trans* (c&t) regulation in the F1 hybrids before (undiff) and after (diff) brite adipogenesis. The percentage relative to all tested genes (of 2,049 in undifferentiated and 2,426 in differentiated samples, see STAR Methods) is marked above the bars. In red, number of genes that are also briteDECoGs.

(H) Log2 fold-change (FC) of gene expression between 129S6 and BL6/J alleles in F1 hybrids versus parental strains before (undiff) and after (diff) brite adipogenesis. Blue, *cis*-regulated; purple, *trans*-regulated; green, *cis* and *trans* (c&t)-regulated genes.

(I–K) Expression overview across F1 hybrids and parental strains for genes encoding TFs. (I) briteDECoGs found to be regulated in *cis*, (J) briteDECoGs with a predicted motif-affinity-affecting SNP at the *Ucp1* locus between high browning strains and BL6/J, and (K) genes expressed before and/or after brite adipogenesis whose binding motifs are overrepresented at genes regulated in *trans* across F1 hybrids. Green, TFs previously involved in brite adipogenesis; purple, TFs tested in our *Ucp1* screen (Figure 4). *, significantly correlated with *Ucp1* across BXD mice; +, significantly DE in 129S6 versus Bl6/J mice; c, regulated in *cis*; dark red, briteDECoG.F1s.

See also Figure S3 and Tables S5, S6, and S7.

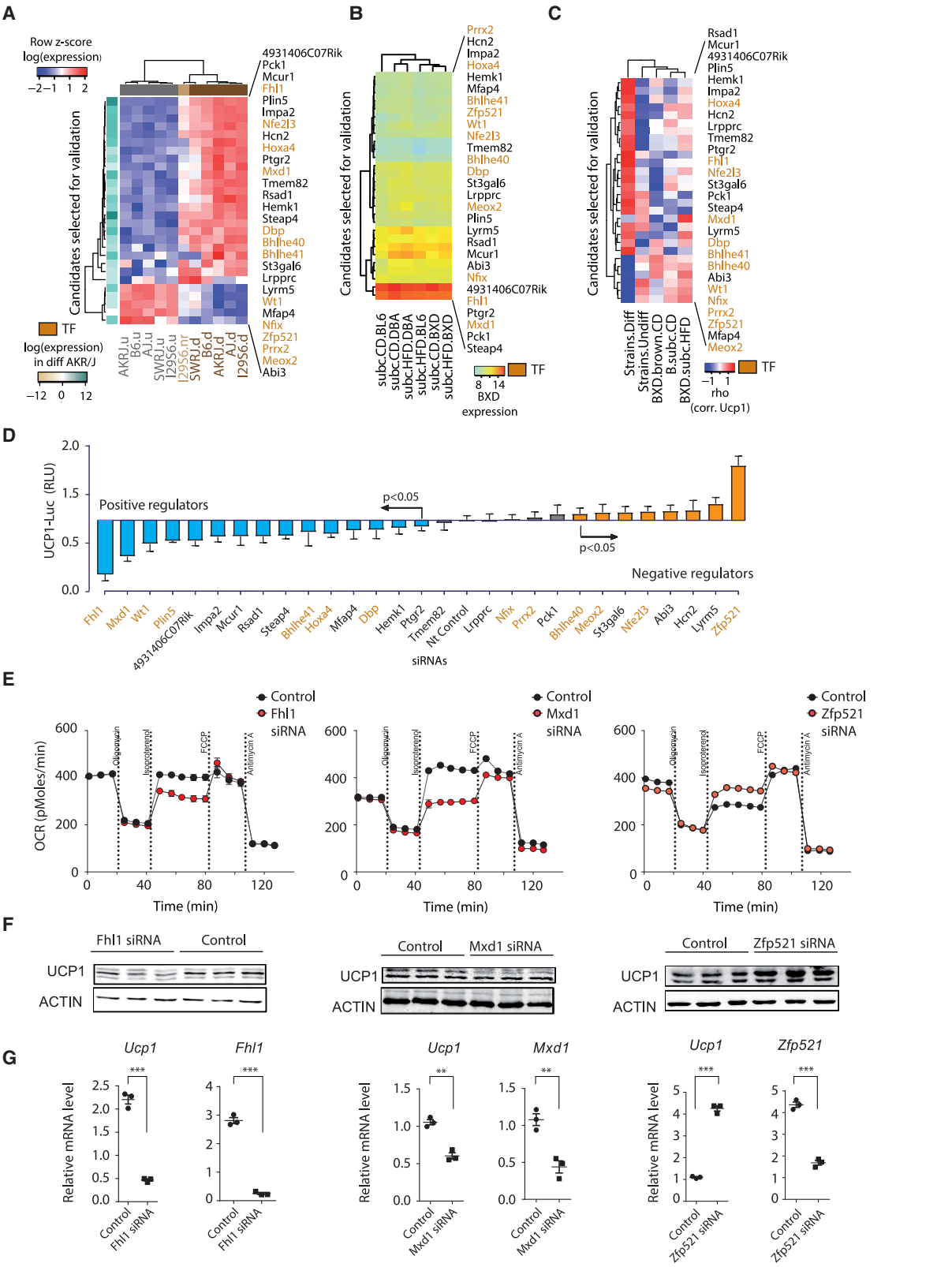

(legend on next page)

that *Mxd1*, *Fhl1*, *Steap4*, *Impa2*, and *Plin5* are required for brite adipocyte differentiation and thermogenic function, while *Zfp521* acts as a negative regulator of these processes.

As an alternative validation strategy, we applied chemical modulators to target metabolic-related and signaling-related candidate genes. In total, nine genes were selected and targeted with corresponding chemical modulators (Figures S4H and S4I). Most notably, stimulation of GPR120 (also known as FFAR4), a G protein-coupled receptor for long-chain unsaturated fatty acids, with a synthetic agonist (GW9508) dramatically induced *Ucp1*-driven luciferase activity to a comparable level as rosiglitazone treatment. While GW9508 is known to act as a dual agonist because it targets both GPR40 and GPR120, GPR40 is not expressed in adipocytes (data not shown), leading us to attribute the GW9508 effects solely to GPR120 activation. Similarly, inhibition of arachidonate 5-lipoxygenase-activating protein (ALOX5AP), also known as 5-lipoxygenase activating protein (FLAP), which facilitates the initial step in leukotriene biosynthesis from arachidonic acid catalyzed by 5-lipoxygenase (5LO), with BAY-X-1005 led to considerable induction of *Ucp1*-driven luciferase activity. We also observed a modest browning effect of retinoid X receptor (RXR) agonist, bexarotene (Bexa). In contrast to these positive effects, inhibiting prolyl hydroxylase domain protein (PHD3, also known as EGLN3) with PHD inhibitor (ethyl-3,4-dihydroxybenzoate) led to downregulation of *Ucp1*-driven luciferase activity. Notably, PHD inhibitor blocked the browning effect of rosiglitazone in a dose-dependent manner (Figure S4I). Although the direct molecular mechanisms by which targeting ALOX5AP and PHD3 act to regulate *Ucp1* are unknown, our results provide a proof-of-principle that a chemical modulator approach can be used to validate candidate genes.

Brite Adipogenic Gene Regulatory Networks

Our genome-wide, strain-specific, and allele-specific expression analyses revealed a large number of genes associated with white fat cell browning, several of which were experimentally validated in functional assays. To gain more detailed insight into the interconnectivity of the identified regulators, we performed KD experiments of the three validated TFs *Fhl1*, *Mxd1*, and *Zfp521*, followed by 3′ RNA-seq-based gene expression analysis (Alpern et al., 2018) at two adipogenic time points (Figure 5A). Overall, we observed few global changes in response to *Zfp521* KD, in contrast to *Fhl1* and *Mxd1* KD, which affected tens-to-hundreds of genes (Figures 5B, S5A, and S5B; Table S8). For *Fhl1* and *Mxd1*, there was an over 2-fold increase in deregulated genes at day 3 compared to day 1, consistent with a failure to activate the brown gene expression program in the KDs. Strikingly, *Ucp1* was one of only two genes affected by the KDs of each of the three TFs at day 3, showing increased levels upon *Zfp521* and decreased ones upon *Mxd1* and *Fhl1* KD, consistent with our previous results (Figures 4D–4G and 5B). The overlap between the transcriptional effects of *Mxd1* and *Fhl1* KD was high, ranging from 15% to 50% of all affected genes (Figure 5B). This was confirmed by the high correlation of fold-changes induced by KDs of *Mxd1* and *Fhl1* but not *Zfp521* (Figure S5C). Over 20% of the genes affected by KDs at day 3 were among briteDECoG.F1s (Figures 5C and S5D), including the KD genes themselves, *Ucp1*, and other canonical brown fat cell markers such as *Cidea* and *Cox8a*.

To obtain a comprehensive overview of TFs active during brite adipogenesis and of their regulatory relation, we performed an integrative transcriptomic and motif overrepresentation analysis using SCENIC (Aibar et al., 2017) (STAR Methods). In brief, we derived a gene co-expression network based on all RNA-seq data (Figure S5E), identified groups of genes regulated by one particular TF (referred to as "regulons"), and estimated activity levels for each TF based on its regulon and its own expression level, as previously described (Aibar et al., 2017) (Tables S9 and S10). For instance, MXD1 was estimated to regulate 28 genes, including the one encoding the TF BHLHE41, validated as activating *Ucp1* in our screen (Figure S5F). Six TFs and one co-regulator were directly linked to *Ucp1* expression: PPARA, PPARD, PPARG, PGC1A, RORA, RXRB, NR1H2, and ZFP110 (Figure S5F), in line with known roles of the PPAR, RXR, and LXR TF families in brown adipogenesis (Korach-André et al., 2011). We further expanded this list by correlating the expression of *Ucp1* with the predicted activity of all TFs, revealing, besides the above-mentioned TFs, the validated candidate DBP on the positive side and the proliferation-related TFs E2F7/8 and MYC on the negative side (Figure S5G). Our analyses revealed the activity pattern of all expressed TFs across differentiation as well as in response to *Mxd1*, *Fhl1*, and *Zfp521* KD (Figures 5E and S5E), with 40 TFs identified as highly active in high browning strains, including the experimentally validated MXD1, BHLHE41, and DBP (Figures 4D and 5E).

Figure 4. Validation of Novel Regulators of Brite Adipogenesis

(A) Gene expression across SVF differentiation for all candidate genes (encoding TFs, orange, and metabolism-related proteins) selected for validation.

(B) Mean *in vivo* gene expression across subcutaneous (subc) and brown fat in BXD strains as well as the two BXD parental lines (BL6 and DBA) for all candidate genes selected for validation.

(C) Correlations of *Ucp1* gene expression with that of selected candidates across SVF differentiation as well as BXD strains.

(D) siRNA-mediated functional screen of selected candidates using *Ucp1*-Luc reporter cells. Blue, validated positive regulators; orange, validated negative regulators. Gene name in orange indicates transcription factor.

(E) Cellular respirometry of *Fhl1*, *Mxd1*, and *Zfp521* knockdown (KD) cells. Time course of oxygen consumption rate (OCR) of targeted gene knockdown cells and nontargeting control adipocytes recorded by microplate-based respirometry (Seahorse XF96 Analyzer) under basal conditions and during successive injection of 5 μM oligomycin, 0.5 μM isoproterenol, 1 μM FCCP, and 5 μM antimycin A. Isoproterenol-stimulated increase of OCR is mediated by UCP1.

(F) Western blot of UCP1 in *Fhl1*, *Mxd1*, and *Zfp521* knockdown (KD) cells.

(G) qPCR-based analysis of *Ucp1* and siRNA-targeted genes in knockdown (KD) cells. t test, *$p < 0.05$, **$p < 0.01$, ***$p < 0.001$.

Error bars represent mean ± SD.

See also Figure S4.

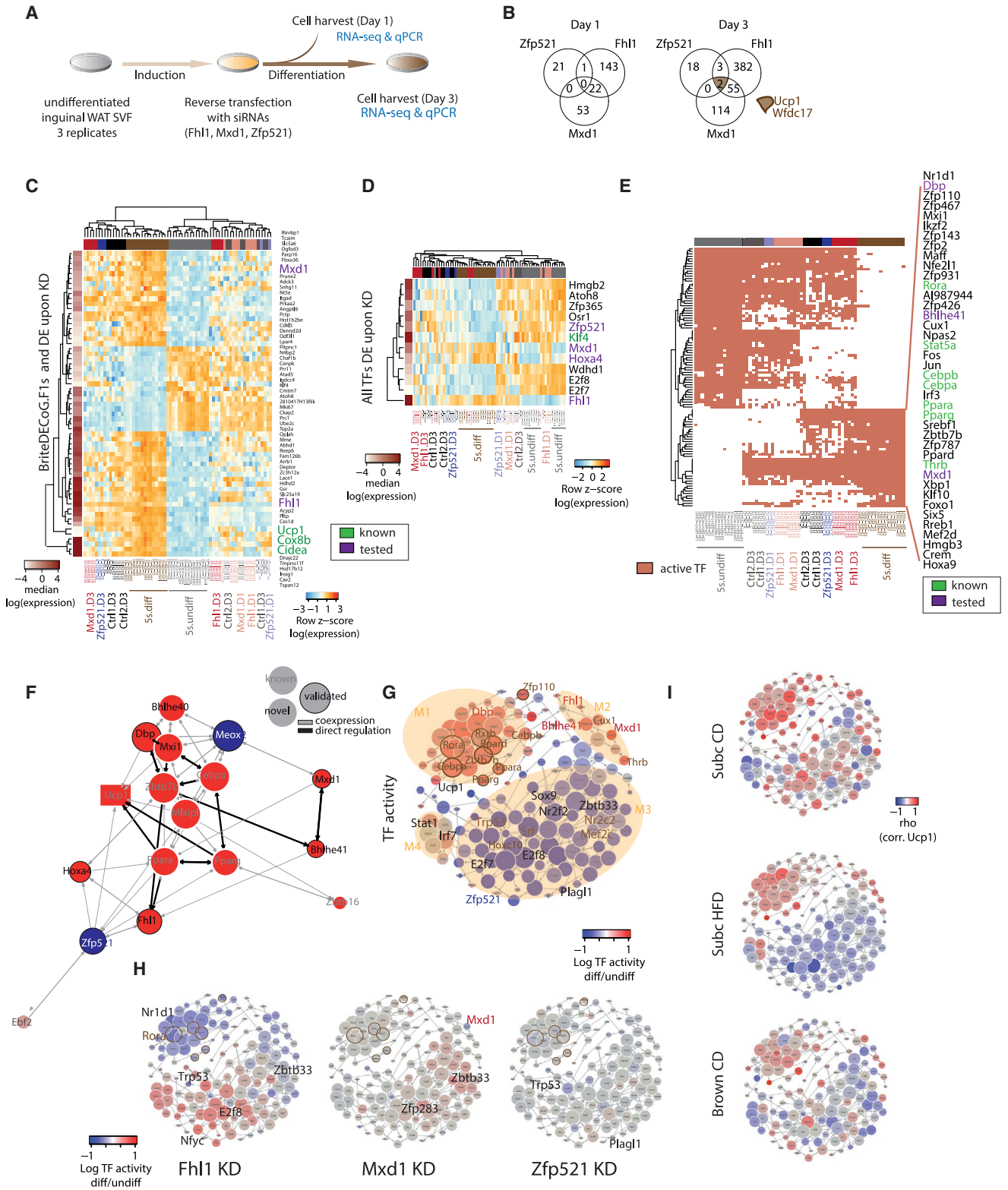

Figure 5. Brite Adipogenic Gene Regulatory Networks

(A) Schematic description of KD experiments of *Mxd1*, *Fhl1*, and *Zfp521*.

(B) Overlap between significantly differentially expressed (DE) genes upon KDs of *Mxd1*, *Fhl1*, and *Zfp521* at days 1 (D1) and 3 (D3), FDR 0.3 and |FC| ≥2.

(legend continued on next page)

We visually summarized the co-expression and co-regulatory information for all (Figure S5I) as well as for a core subset of TFs of interest (Figure 5F), including (1) known core (brown) adipogenesis regulators, (2) briteDECoG.F1s.UP predicted to directly regulate *Ucp1* expression (Figures 3J and S5G), and (3) validated regulators (Figure 4D). While the canonical adipogenic TFs PPARA and PPARG emerged as the sole direct inputs into *Ucp1* expression, they were linked through CEBPA and ZBTB7B to the novel positive regulators MXI1, DBP, and FHL1, forming a closely connected module (Figure 5F). A mutually regulatory relation with BHLEH41 connected MXD1 through ZBTB7B to the network (Figure 5F). The discovered negative regulator MEOX2 was closely associated to the highly connected module, and ZFP521 was directly linked to *Ucp1* as well as to the established adipogenic TFs PPARA, PPARG, and the hereby validated FHL1 (Figure 5F). With the exception of EBF2, all these factors were highly DE upon differentiation, and a majority also changed upon KD of *Mxd1*, *Fhl1*, and *Zfp521*, respectively (Figure S5J).

To position these TFs in a broader context of brite adipogenesis, we displayed all direct regulatory connections among all active TFs as well as *Ucp1* and the hereby validated TFs *Fhl1* and *Zfp521*, which had no assigned regulon (Figures 5G and S5K; STAR Methods). A closely connected group of TFs, including the known RORA, RXRB, PPARG, PPARA, but also the hereby validated DBP, emerged as closely linked to *Ucp1* expression (module 1, M1, Figure 5G). MXD1, FHL1, and BHLHE41 were more loosely associated with this group of TFs (module 2, M2) and were linked to a third major group containing the identified negative regulator ZFP521, the cell-cycle regulators E2F7/8, and the imprinted factor PLAGL1 (module 3, M3). The TF activity patterns across differentiation of both high and low browning strains, as well as F1 mice, were highly consistent with their expression levels, with a trend toward lower activity differences in BL6/J and SWR/J mice compared to high browning genetic backgrounds (Figures S5J–S5L). *Fhl1* KD resulted in the strongest expression and activity changes in the network, as the entire DBP-module (M1) was downregulated and the E2F8-module (M3) was upregulated. *Mxd1* KD induced similar, but much fewer striking changes: individual TFs such as E2F8, HOXB6, ZFP283, and ZBTB33 stood out as highly increasing their expression and/or activity. Finally, *Zfp521* KD induced downregulation of the genes encoding several E2F8-module TFs such as E2F7, CTCF, TRP53, and PLAGL1, but also, interestingly, upregulation of *Fhl1*, consistent with an inverse regulatory relation between the two factors, as also suggested from the co-expression network (Figures 5H and S5M; Table S9).

Finally, we asked how our *in vitro*-derived network translated to *in vivo* data by enquiring the BXD data for gene expression correlations between network nodes and *Ucp1* (Figure 5I). Strikingly, members of the *Ucp1*-proximal DBP module were highly correlated to *Ucp1* across the strains, with higher correlations in subcutaneous samples, suggesting that this module is also central to *in vivo* brite adipogenesis and thus functionally relevant.

Adding further confidence to the derived gene regulatory network, multiple of its less established member genes have been experimentally validated in recent studies. For example, ZBTB7B, which is linked to M1 in our network, has been reported as a potent driver of brown fat development and thermogenesis and cold-induced brite adipocytes formation (Li et al., 2017a). Multiple genes in M3, such as HOXC10, P53, NR2C2, SRF, MEF2C, and NR2F2 have been shown to negatively regulate *Ucp1* (Kang et al., 2011; Li et al., 2009; Ng et al., 2017). These results provide further support for the relevance of our gene regulatory network.

DISCUSSION

Browning of white adipose tissue is a highly variable trait that is under complex genetic control (Guerra et al., 1998). In this study, we have undertaken a detailed and comprehensive dissection of the cell-intrinsic genetic and regulatory mechanisms driving brite adipogenesis. In contrast to studies employing mice with genetic modifications of selected candidate genes, we exploited the broad natural genetic and phenotypic variation of inbred mouse strains. Our systematic and unbiased approach revealed novel regulators as well as a core regulatory network that contribute to this natural variation in browning propensity.

To dissect the sources of strain variation in *Ucp1* expression, we mapped out *cis*- and/or *trans*-regulatory effects in both precursor cells and differentiated adipocytes. Through allele-specific expression analyses, we found that *cis*-regulatory effects were the primary mechanism of gene regulatory divergence between BL6 and 129 primary cultured inguinal adipocytes, in line with previous studies in distinct cell types/systems and strains (Goncalves et al., 2012; Shen et al., 2014; Wittkopp and Kalay, 2011). Notably, *Ucp1* also represented a case of *cis*-acting imbalance, favoring 129 alleles over B6 ones. This finding

(C–E) Overview of gene expression (row, normalized log2 expression) across brite adipogenesis and gene perturbations of DE briteDECoG.F1s (C) and TFs (D) upon *Mxd1*, *Fhl1*, or *Zfp521* KD.

(E) Overview of binary TF activity (red, active) across brite adipogenesis and gene perturbations of all TFs showing a change in activity across differentiation in the three high browning strains (STAR Methods). Green, genes previously involved in brite adipogenesis; purple, genes tested in our *Ucp1* screen (Figure 4). White-to-red median log2 expression per gene across samples.

(F–I) Force-directed network topology of a core set of TFs of interest (STAR Methods) (F) and of all TFs showing dynamic activity across the tested strains and conditions (nodes), as well as *Ucp1*, and the validated regulators *Mxd1*, *Fhl1*, and *Zfp521* (G–I). Node sizes are proportional to linkage number (number of connections), arrows indicate the regulatory direction.

(F) Blue-to-red, difference in gene expression between differentiated and undifferentiated 129S6 samples; gray, co-expression-based links; black, direct regulatory links. Known, novel, and validated candidate are highlighted.

(G–I) Only direct regulatory links are included. Blue-to-red: difference in TF activity between differentiated and undifferentiated 129S6 samples (G) and *Mxd1*, *Fhl1*, and *Zfp521* samples (H).

(I) Blue-to-red, correlation to *Ucp1* across BXD samples.

See also Figure S5 and Tables S8, S9, and S10.

is consistent with a recent study, which demonstrated that *Ucp1* upstream regulatory elements favor PPARγ binding to the 129 locus over the BL6 locus in iWAT of B6x129 (129S1/SvImJ) F1-intercrossed mice (Soccio et al., 2017). These results demonstrated that *cis* variants in the 129 *Ucp1* allele determine the differential binding occupancy of PPAR. Nevertheless, PPARG binding differences were not really related to SNPs in *Ucp1* PPARG binding sites. Therefore, the PPARG binding occupancy that varies between strains must be caused by the proximal presence of other TFs that bind to the *Ucp1* locus, consistent with the notion that PPARG binding depends on local chromatin accessibility as mediated by other collaborating TFs (Grossman et al., 2017; Hoffmann et al., 2013; Simicevic et al., 2013). In an attempt to explore the SNPs at the *Ucp1* locus that likely affect TF binding activity, we found a few TFs with altered predicted binding motif affinity. Most notably, the TF ChREBP (encoded by *Mlxipl*), recently shown to directly bind to the distal regulatory region of *Ucp1* and to regulate *Ucp1* expression in response to T3 and glucose (Katz et al., 2018), is among these TFs (Figures 3J and 5F). Interestingly, one of our identified and validated TFs, BHLHE41, also has a potential differential binding affinity favoring the 129-Ucp1 allele over the BL6 one.

Besides UCP1, many TFs identified in our study as associated with the brite regulatory program (briteDECoG.F1s) were themselves regulated in *cis*, including THRB, GRLH1, WT1, ZBTB7C, and ZBTB16. While the latter (ZBTB16) (Plaisier et al., 2012) has already demonstrated roles in *Ucp1* regulation, the former (THRB, GRLH1, WT1, and ZBTB7C) have not previously been implicated in browning. We now directly validate one of these factors, WT1, in our screen. It is possible that differences in the levels of one of these TFs are responsible for the measured *trans* effects. Overall, our results support a model in which *cis*-acting variants lead to local coordination of TF occupancies, thereby contributing to the observed strain variation in browning propensity.

More generally, our comparative approach revealed several known regulators of white fat browning but also dozens of candidates that were successfully validated, including the TF-encoding genes (*Mxd1*, *Fhl1*, *Wt1*, *Hoxa4*, *Dbp*, *Bhlhe41*, *Zfp521*, and *Meox2*), metabolism-related genes (*Plin5*, *Impa2*, *Steap4*, and *Ptgr2*), mitochondria-associated genes (*Ccdc90a*, *Rsad1*, and *Hemk1*), and signaling-related genes and drug targets (*Ffar4*, *Alox5ap*, and *Egln3*). Importantly, we not only demonstrated that these genes are essential for *Ucp1* regulation during brite adipogenesis, but also validated *Fhl1*, *Mxd1*, *Zfp521*, *Steap4*, *Impa2*, and *Plin5* at a functional level. It should be noted that we have applied multiple validation strategies, ranging from siRNA-based screening using *Ucp1*-reporter cells derived from a mouse strain (C57BL/6N) not implemented *a priori* in the integrative analysis, over functional validation by cellular-based respirometry to pharmacological modulation. Among our validated genes, *Zfp521* has been previously demonstrated to act as an anti-adipocyte commitment factor via its interaction with EBF1 resulting in the inhibition of the Zfp423-Ebf1 functional complex and possibly also by inhibiting *Zfp423* expression (Kang et al., 2012). However, its role in brown and brite adipogenesis had so far remained unclear. Here, we demonstrate that *Zfp521* is involved in *Ucp1* regulation during brite adipogenesis, independent of its role in adipogenic regulation. Consistent with our results, *Fhl1* was previously reported to be associated with a brite-selective super-enhancer and to be required for browning of human white adipocytes (Loft et al., 2015). Ectopic expression of MXD1 in preadipocytes resulted in inhibition of adipogenesis in 3T3-L1 cells (Pulverer et al., 2000).

While the exact individual molecular mechanisms by which these factors modulate brite adipogenesis remain to be elucidated, our large-scale datasets provided the opportunity to derive a comprehensive overview of the inter-connectedness of TFs regulating this process. Our transcriptional network analyses based on brite adipogenic and perturbation transcriptomes as well as TF binding site (TFBS) information revealed up to four distinct regulatory modules that underlie brite adipogenesis. One major module that is positively linked to *Ucp1* expression was highly inter-connected between previously known (brite) adipogenic regulators such as PPARG, RXRB, and ZBTB7B, but also identified new ones such as DBP and BHLHE41, while another large one contained the identified negative regulator ZFP521 among an entire range of known and candidate repressive TFs. Notably, several TFs in these modules have been previously (PPARG, PPARA, RORA, RXRB, ZBTB7B) or now (DBP, BHLHE41, MXD1, FHL1, ZFP521) validated as critical mediators of brite adipogenesis. Genes such as HOXC10, P53, NR2C2, SRF, MEF2C, and NR2F2 have been demonstrated as negative regulators of *Ucp1* regulation. Of note, mice lacking the nuclear receptors NR2C2 or NR2F2 displayed increased *Ucp1* expression in white fat depots, supporting the *in vivo* relevance of the identified regulatory network (Kang et al., 2011; Li et al., 2009). Considering the large number of genes that influence *Ucp1* expression, our study is consistent with the notion that synergistic interactions among causal variants with tiny effect sizes lead to large differences in *Ucp1* expression (Koza et al., 2000; Xue et al., 2005). Thus, focusing on pathways and networks rather than pinpointing individual genes may constitute a more efficient strategy in designing therapeutic strategies to promote the browning of white fat. It must be mentioned that there is growing evidence indicating multiple subtypes of thermogenic adipocytes with distinct cellular origins, depending on the nature of external stimuli, such as cold acclimation, rosiglitazone, and roscovitine treatment (Wang et al., 2016). Therefore, to what extent our rosiglitazone-induced browning *in vitro* truly represent brite adipogenesis *in vivo* is unknown and warrants further investigation.

In sum, our study highlights the power of a systems-genetics approach in the molecular dissection of phenotypic variation and the identification of causal genes and regulatory relationships. Combining comparative transcriptome, perturbation-based assays, and gene network analyses, our results constitute, to our knowledge, the most comprehensive attempt to define the regulatory network underlying white fat browning. Additional studies such as epigenomic profiling will help draw a more complete canvas of the sources of gene expression variability in this system. *In vivo* validation of our identified factors and regulatory network using genetically modified animal models will undoubtedly provide further invaluable insights. In the long run, a full understanding of the molecular architecture underlying brite cell recruitment could facilitate the development of therapeutic approaches for combating metabolic imbalance.

STAR★METHODS

Detailed methods are provided in the online version of this paper and include the following:

- KEY RESOURCES TABLE
- LEAD CONTACT AND MATERIALS AVAILABILITY
- EXPERIMENTAL MODEL AND SUBJECT DETAILS
- METHOD DETAILS
  - Primary Cell Isolation and Culture
- QUANTIFICATION AND STATISTICAL ANALYSIS
- DATA AND CODE AVAILABILITY

SUPPLEMENTAL INFORMATION

Supplemental Information can be found online at https://doi.org/10.1016/j.celrep.2019.11.053.

ACKNOWLEDGMENTS

We thank Prof. Johan Auwerx for providing access to the BXD data and the EPFL Gene Expression Core Facility sequencing support, as well as the VITAL-IT platform (University of Lausanne, Swiss Institute of Bioinformatics) for computational support. We would like also thank Hui Wang for providing the *Ucp1*-luc reporter mice for primary cell isolation and Dr. Marco Groth and Dr. Karol Szafranski at the Fritz Lipman Institute for Age Research (Jena, Germany) for help with RNA sequencing in the early stage of this project. This research was supported by the German Research Society (KL 973/12-1), seed money from the German Obesity Competence Network (BMBF 01GI1325), the Else Kröner-Fresenius-Stiftung (EKFS), the Human Frontier Science Program LT001032/2013 (to P.C.S.), the Swiss National Science Foundation (31003A_138323 and 31003A_162735), and institutional support from the Swiss Federal Institute of Technology in Lausanne (EPFL).

AUTHOR CONTRIBUTIONS

Y.L., P.C.S., B.D., and M.K. designed the study and wrote the manuscript. Y.L. conducted all primary cell cultures, screening, siRNA-based knockdown, and cellular respirometry experiments. P.C.S. conducted all transcriptomics-related analyses. J.R. performed some of the RNA-seq experiments. A.B.-H. helped with some experiments. S.M. performed the western blots. T.F. helped with RNA sequencing and analysis. All authors read and approved the final manuscript.

DECLARATION OF INTERESTS

The authors declare no competing interests.

Received: June 11, 2019
Revised: October 2, 2019
Accepted: November 13, 2019
Published: December 17, 2019

REFERENCES

Aibar, S., González-Blas, C.B., Moerman, T., Huynh-Thu, V.A., Imrichova, H., Hulselmans, G., Rambow, F., Marine, J.-C., Geurts, P., Aerts, J., et al. (2017). SCENIC: single-cell regulatory network inference and clustering. Nat. Methods *14*, 1083–1086.

Almind, K., Manieri, M., Sivitz, W.I., Cinti, S., and Kahn, C.R. (2007). Ectopic brown adipose tissue in muscle provides a mechanism for differences in risk of metabolic syndrome in mice. Proc. Natl. Acad. Sci. USA *104*, 2366–2371.

Alpern, D., Gardeux, V., Russeil, J., and Deplancke, B. (2018). Time- and cost-efficient high-throughput transcriptomics enabled by Bulk RNA Barcoding and sequencing. bioRxiv. https://doi.org/10.1101/256594.

Alpern, D., Gardeux, V., Russeil, J., Mangeat, B., Meireles-Filho, A.C.A., Breysse, R., Hacker, D., and Deplancke, B. (2019). BRB-seq: ultra-affordable high-throughput transcriptomics enabled by bulk RNA barcoding and sequencing. Genome Biol. *20*, 71.

Anderson, C.M., Kazantzis, M., Wang, J., Venkatraman, S., Goncalves, R.L., Quinlan, C.L., Ng, R., Jastroch, M., Benjamin, D.I., Nie, B., et al. (2015). Dependence of brown adipose tissue function on CD36-mediated coenzyme Q uptake. Cell Rep. *10*, 505–515.

Andreux, P.A., Williams, E.G., Koutnikova, H., Houtkooper, R.H., Champy, M.F., Henry, H., Schoonjans, K., Williams, R.W., and Auwerx, J. (2012). Systems genetics of metabolism: the use of the BXD murine reference panel for multiscalar integration of traits. Cell *150*, 1287–1299.

Bartelt, A., Bruns, O.T., Reimer, R., Hohenberg, H., Ittrich, H., Peldschus, K., Kaul, M.G., Tromsdorf, U.I., Weller, H., Waurisch, C., et al. (2011). Brown adipose tissue activity controls triglyceride clearance. Nat. Med. *17*, 200–205.

Betz, M.J., and Enerback, S. (2017). Targeting thermogenesis in brown fat and muscle to treat obesity and metabolic disease. Nat. Rev. Endocrinol. *14*, 77–87.

Birsoy, K., Chen, Z., and Friedman, J. (2008). Transcriptional regulation of adipogenesis by KLF4. Cell Metab. *7*, 339–347.

Burl, R.B., Ramseyer, V.D., Rondini, E.A., Pique-Regi, R., Lee, Y.H., and Granneman, J.G. (2018). Deconstructing Adipogenesis Induced by β3-Adrenergic Receptor Activation with Single-Cell Expression Profiling. Cell Metab. *28*, 300–309.

Cheng, Y., Jiang, L., Keipert, S., Zhang, S., Hauser, A., Graf, E., Strom, T., Tschöp, M., Jastroch, M., and Perocchi, F. (2018). Prediction of Adipose Browning Capacity by Systematic Integration of Transcriptional Profiles. Cell Rep. *23*, 3112–3125.

Deplancke, B., Alpern, D., and Gardeux, V. (2016). The Genetics of Transcription Factor DNA Binding Variation. Cell *166*, 538–554.

Dobin, A., Davis, C.A., Schlesinger, F., Drenkow, J., Zaleski, C., Jha, S., Batut, P., Chaisson, M., and Gingeras, T.R. (2013). STAR: ultrafast universal RNA-seq aligner. Bioinformatics *29*, 15–21.

Goncalves, A., Leigh-Brown, S., Thybert, D., Stefflova, K., Turro, E., Flicek, P., Brazma, A., Odom, D.T., and Marioni, J.C. (2012). Extensive compensatory cis-trans regulation in the evolution of mouse gene expression. Genome Res. *22*, 2376–2384.

Grossman, S.R., Zhang, X., Wang, L., Engreitz, J., Melnikov, A., Rogov, P., Tewhey, R., Isakova, A., Deplancke, B., Bernstein, B.E., et al. (2017). Systematic dissection of genomic features determining transcription factor binding and enhancer function. Proc. Natl. Acad. Sci. USA *114*, E1291–E1300.

Guerra, C., Koza, R.A., Yamashita, H., Walsh, K., and Kozak, L.P. (1998). Emergence of brown adipocytes in white fat in mice is under genetic control. Effects on body weight and adiposity. J. Clin. Invest. *102*, 412–420.

Hampton, M., Melvin, R.G., and Andrews, M.T. (2013). Transcriptomic analysis of brown adipose tissue across the physiological extremes of natural hibernation. PLoS ONE *8*, e85157.

Harms, M., and Seale, P. (2013). Brown and beige fat: development, function and therapeutic potential. Nat. Med. *19*, 1252–1263.

Hoffmann, C., Zimmermann, A., Hinney, A., Volckmar, A.L., Jarrett, H.W., Fromme, T., and Klingenspor, M. (2013). A novel SP1/SP3 dependent intronic enhancer governing transcription of the UCP3 gene in brown adipocytes. PLoS ONE *8*, e83426.

Kang, H.S., Okamoto, K., Kim, Y.S., Takeda, Y., Bortner, C.D., Dang, H., Wada, T., Xie, W., Yang, X.P., Liao, G., and Jetten, A.M. (2011). Nuclear orphan receptor TAK1/TR4-deficient mice are protected against obesity-linked inflammation, hepatic steatosis, and insulin resistance. Diabetes *60*, 177–188.

Kang, S., Akerblad, P., Kiviranta, R., Gupta, R.K., Kajimura, S., Griffin, M.J., Min, J., Baron, R., and Rosen, E.D. (2012). Regulation of early adipose commitment by Zfp521. PLoS Biol. *10*, e1001433.

Katz, L.S., Xu, S., Ge, K., Scott, D.K., and Gershengorn, M.C. (2018). T3 and Glucose Coordinately Stimulate ChREBP-Mediated Ucp1 Expression in Brown Adipocytes From Male Mice. Endocrinology *159*, 557–569.

Kless, C., Rink, N., Rozman, J., and Klingenspor, M. (2017). Proximate causes for diet-induced obesity in laboratory mice: a case study. Eur. J. Clin. Nutr. *71*, 306–317.

Korach-André, M., Archer, A., Barros, R.P., Parini, P., and Gustafsson, J.A. (2011). Both liver-X receptor (LXR) isoforms control energy expenditure by regulating brown adipose tissue activity. Proc. Natl. Acad. Sci. USA *108*, 403–408.

Koza, R.A., Hohmann, S.M., Guerra, C., Rossmeisl, M., and Kozak, L.P. (2000). Synergistic gene interactions control the induction of the mitochondrial uncoupling protein (Ucp1) gene in white fat tissue. J. Biol. Chem. *275*, 34486–34492.

Kozak, L.P., and Koza, R.A. (2010). The genetics of brown adipose tissue. Prog. Mol. Biol. Transl. Sci. *94*, 75–123.

Li, L., Xie, X., Qin, J., Jeha, G.S., Saha, P.K., Yan, J., Haueter, C.M., Chan, L., Tsai, S.Y., and Tsai, M.J. (2009). The nuclear orphan receptor COUP-TFII plays an essential role in adipogenesis, glucose homeostasis, and energy metabolism. Cell Metab. *9*, 77–87.

Li, Y., Lasar, D., Fromme, T., and Klingenspor, M. (2013). White, brite, and brown adipocytes: the evolution and function of a heater organ in mammals. Can. J. Zool. *92*, 615–626.

Li, Y., Bolze, F., Fromme, T., and Klingenspor, M. (2014a). Intrinsic differences in BRITE adipogenesis of primary adipocytes from two different mouse strains. Biochim. Biophys. Acta *1841*, 1345–1352.

Li, Y., Fromme, T., Schweizer, S., Schöttl, T., and Klingenspor, M. (2014b). Taking control over intracellular fatty acid levels is essential for the analysis of thermogenic function in cultured primary brown and brite/beige adipocytes. EMBO Rep. *15*, 1069–1076.

Li, S., Mi, L., Yu, L., Yu, Q., Liu, T., Wang, G.X., Zhao, X.Y., Wu, J., and Lin, J.D. (2017a). Zbtb7b engages the long noncoding RNA Blnc1 to drive brown and beige fat development and thermogenesis. Proc. Natl. Acad. Sci. USA *114*, E7111–E7120.

Li, Y., Fromme, T., and Klingenspor, M. (2017b). Meaningful respirometric measurements of UCP1-mediated thermogenesis. Biochimie *134*, 56–61.

Li, Y., Schnabl, K., Gabler, S.M., Willershauser, M., Reber, J., Karlas, A., Laurila, S., Lahesmaa, M., U Din, M., Bast-Habersbrunner, A., et al. (2018). Secretin-Activated Brown Fat Mediates Prandial Thermogenesis to Induce Satiation. Cell *175*, 1561–1574.

Loft, A., Forss, I., Siersbæk, M.S., Schmidt, S.F., Larsen, A.S., Madsen, J.G., Pisani, D.F., Nielsen, R., Aagaard, M.M., Mathison, A., et al. (2015). Browning of human adipocytes requires KLF11 and reprogramming of PPARγ superenhancers. Genes Dev. *29*, 7–22.

Martin, M. (2011). Cutadapt removes adapter sequences from high-throughput sequencing reads. EMBnet.journal *17*. https://doi.org/10.14806/ej.17.1.200.

McDonald, M.E., Li, C., Bian, H., Smith, B.D., Layne, M.D., and Farmer, S.R. (2015). Myocardin-related transcription factor A regulates conversion of progenitors to beige adipocytes. Cell *160*, 105–118.

Ng, M., Fleming, T., Robinson, M., Thomson, B., Graetz, N., Margono, C., Mullany, E.C., Biryukov, S., Abbafati, C., Abera, S.F., et al. (2014). Global, regional, and national prevalence of overweight and obesity in children and adults during 1980-2013: a systematic analysis for the Global Burden of Disease Study 2013. Lancet *384*, 766–781.

Ng, Y., Tan, S.X., Chia, S.Y., Tan, H.Y., Gun, S.Y., Sun, L., Hong, W., and Han, W. (2017). HOXC10 suppresses browning of white adipose tissues. Exp. Mol. Med. *49*, e292.

Park, Y.-K., Wang, L., Giampietro, A., Lai, B., Lee, J.-E., and Ge, K. (2017). Distinct Roles of Transcription Factors KLF4, Krox20, and Peroxisome Proliferator-Activated Receptor γ in Adipogenesis. Mol. Cell. Biol. *37*, e00554-16.

Plaisier, C.L., Bennett, B.J., He, A., Guan, B., Lusis, A.J., Reue, K., and Vergnes, L. (2012). Zbtb16 has a role in brown adipocyte bioenergetics. Nutr. Diabetes *2*, e46.

Pradhan, R.N., Bues, J.J., Gardeux, V., Schwalie, P.C., Alpern, D., Chen, W., Russeil, J., Raghav, S.K., and Deplancke, B. (2017a). Dissecting the brown adipogenic regulatory network using integrative genomics. Sci. Rep. *7*, 42130.

Pradhan, R.N., Zachara, M., and Deplancke, B. (2017b). A systems perspective on brown adipogenesis and metabolic activation. Obes. Rev. *18* (*Suppl 1*), 65–81.

Pulverer, B., Sommer, A., McArthur, G.A., Eisenman, R.N., and Lüscher, B. (2000). Analysis of Myc/Max/Mad network members in adipogenesis: inhibition of the proliferative burst and differentiation by ectopically expressed Mad1. J. Cell. Physiol. *183*, 399–410.

Rajakumari, S., Wu, J., Ishibashi, J., Lim, H.W., Giang, A.H., Won, K.J., Reed, R.R., and Seale, P. (2013). EBF2 determines and maintains brown adipocyte identity. Cell Metab. *17*, 562–574.

Ritchie, M.E., Phipson, B., Wu, D., Hu, Y., Law, C.W., Shi, W., and Smyth, G.K. (2015). limma powers differential expression analyses for RNA-sequencing and microarray studies. Nucleic Acids Res. *43*, e47.

Scheele, C., and Nielsen, S. (2017). Metabolic regulation and the anti-obesity perspectives of human brown fat. Redox Biol. *12*, 770–775.

Schmieder, R., and Edwards, R. (2011). Quality control and preprocessing of metagenomic datasets. Bioinformatics *27*, 863–864.

Schulz, T.J., Huang, T.L., Tran, T.T., Zhang, H., Townsend, K.L., Shadrach, J.L., Cerletti, M., McDougall, L.E., Giorgadze, N., Tchkonia, T., et al. (2011). Identification of inducible brown adipocyte progenitors residing in skeletal muscle and white fat. Proc. Natl. Acad. Sci. USA *108*, 143–148.

Shemer, R., Birger, Y., Riggs, A.D., and Razin, A. (1997). Structure of the imprinted mouse Snrpn gene and establishment of its parental-specific methylation pattern. Proc. Natl. Acad. Sci. USA *94*, 10267–10272.

Shen, S.Q., Turro, E., and Corbo, J.C. (2014). Hybrid mice reveal parent-of-origin and Cis- and trans-regulatory effects in the retina. PLoS ONE *9*, e109382.

Sidossis, L., and Kajimura, S. (2015). Brown and beige fat in humans: thermogenic adipocytes that control energy and glucose homeostasis. J. Clin. Invest. *125*, 478–486.

Simicevic, J., Schmid, A.W., Gilardoni, P.A., Zoller, B., Raghav, S.K., Krier, I., Gubelmann, C., Lisacek, F., Naef, F., Moniatte, M., and Deplancke, B. (2013). Absolute quantification of transcription factors during cellular differentiation using multiplexed targeted proteomics. Nat. Methods *10*, 570–576.

Soccio, R.E., Li, Z., Chen, E.R., Foong, Y.H., Benson, K.K., Dispirito, J.R., Mullican, S.E., Emmett, M.J., Briggs, E.R., Peed, L.C., et al. (2017). Targeting PPARγ in the epigenome rescues genetic metabolic defects in mice. J. Clin. Invest. *127*, 1451–1462.

Tseng, Y.H., Cypess, A.M., and Kahn, C.R. (2010). Cellular bioenergetics as a target for obesity therapy. Nat. Rev. Drug Discov. *9*, 465–482.

Turro, E., Su, S.Y., Gonçalves, Â., Coin, L.J.M., Richardson, S., and Lewin, A. (2011). Haplotype and isoform specific expression estimation using multi-mapping RNA-seq reads. Genome Biol. *12*, R13.

Turro, E., Astle, W.J., and Tavaré, S. (2014). Flexible analysis of RNA-seq data using mixed effects models. Bioinformatics *30*, 180–188.

Ussar, S., Lee, K.Y., Dankel, S.N., Boucher, J., Haering, M.F., Kleinridders, A., Thomou, T., Xue, R., Macotela, Y., Cypess, A.M., et al. (2014). ASC-1, PAT2, and P2RX5 are cell surface markers for white, beige, and brown adipocytes. Sci. Transl. Med. *6*, 247ra103.

Varrault, A., Gueydan, C., Delalbre, A., Bellmann, A., Houssami, S., Aknin, C., Severac, D., Chotard, L., Kahli, M., Le Digarcher, A., et al. (2006). Zac1 regulates an imprinted gene network critically involved in the control of embryonic growth. Dev. Cell *11*, 711–722.

Vitali, A., Murano, I., Zingaretti, M.C., Frontini, A., Ricquier, D., and Cinti, S. (2012). The adipose organ of obesity-prone C57BL/6J mice is composed of mixed white and brown adipocytes. J. Lipid Res. *53*, 619–629.

Wang, G.X., Zhao, X.Y., Meng, Z.X., Kern, M., Dietrich, A., Chen, Z., Cozacov, Z., Zhou, D., Okunade, A.L., Su, X., et al. (2014). The brown fat-enriched secreted factor Nrg4 preserves metabolic homeostasis through attenuation of hepatic lipogenesis. Nat. Med. *20*, 1436–1443.

Wang, H., Liu, L., Lin, J.Z., Aprahamian, T.R., and Farmer, S.R. (2016). Browning of White Adipose Tissue with Roscovitine Induces a Distinct Population of UCP1^{+} Adipocytes. Cell Metab. *24*, 835–847.

Wang, H., Willershauser, M., Karlas, A., Gorpas, D., Reber, J., Ntziachristos, V., Maurer, S., Fromme, T., Li, Y., and Klingenspor, M. (2019). A dual Ucp1 reporter mouse model for imaging and quantitation of brown and brite fat recruitment. Mol. Metab. *20*, 14–27.

Watson, P.M., Commins, S.P., Beiler, R.J., Hatcher, H.C., and Gettys, T.W. (2000). Differential regulation of leptin expression and function in A/J vs. C57BL/6J mice during diet-induced obesity. Am. J. Physiol. Endocrinol. Metab. *279*, E356–E365.

West, D.B., Waguespack, J., York, B., Goudey-Lefevre, J., and Price, R.A. (1994). Genetics of dietary obesity in AKR/J x SWR/J mice: segregation of the trait and identification of a linked locus on chromosome 4. Mamm. Genome *5*, 546–552.

Wittkopp, P.J., and Kalay, G. (2011). Cis-regulatory elements: molecular mechanisms and evolutionary processes underlying divergence. Nat. Rev. Genet. *13*, 59–69.

Wu, Y., Williams, E.G., Dubuis, S., Mottis, A., Jovaisaite, V., Houten, S.M., Argmann, C.A., Faridi, P., Wolski, W., Kutalik, Z., et al. (2014). Multilayered genetic and omics dissection of mitochondrial activity in a mouse reference population. Cell *158*, 1415–1430.

Xue, B., Coulter, A., Rim, J.S., Koza, R.A., and Kozak, L.P. (2005). Transcriptional synergy and the regulation of Ucp1 during brown adipocyte induction in white fat depots. Mol. Cell. Biol. *25*, 8311–8322.

Yang, L., Li, X., Tang, H., Gao, Z., Zhang, K., and Sun, K. (2019). A Unique Role of Carboxylesterase 3 (Ces3) in β-Adrenergic Signaling-Stimulated Thermogenesis. Diabetes *68*, 1178–1196.

Yoneshiro, T., Wang, Q., Tajima, K., Matsushita, M., Maki, H., Igarashi, K., Dai, Z., White, P.J., McGarrah, R.W., Ilkayeva, O.R., et al. (2019). BCAA catabolism in brown fat controls energy homeostasis through SLC25A44. Nature *572*, 614–619.

Zerbino, D.R., Achuthan, P., Akanni, W., Amode, M.R., Barrell, D., Bhai, J., Billis, K., Cummins, C., Gall, A., Girón, C.G., et al. (2018). Ensembl 2018. Nucleic Acids Res. *46* (*D1*), D754–D761.

STAR★METHODS

KEY RESOURCES TABLE

REAGENT or RESOURCE	SOURCE	IDENTIFIER
Antibodies		
anti-UCP1	Custom made	N/A
anti-ACTIN	Millipore	RRID: AB_2223041: Cat# MAB1501
Chemicals, Peptides, and Recombinant Proteins		
Isobutylmethylxanthine	Sigma-Aldrich	Cat# I5879
Indomethacin	Sigma-Aldrich	Cat# I7378
Dexamethasone	Sigma-Aldrich	Cat# D4902
Insulin	Sigma-Aldrich	Cat# I9278-5ML
T3	Sigma-Aldrich	Cat# T6397
Propranolol hydrochlorid	Sigma-Aldrich	Cat# P8688
Bovine serum albumin (BSA) Fatty Acid Free	Sigma-Aldrich	Cat# A3803-100G
Isoproterenol	Sigma-Aldrich	Cat# I6504-100MG
Oligomycin	Sigma-Aldrich	Cat# O4876-5mg
Antimycin A	Sigma-Aldrich	Cat# A8674
Collagenase A	Biochrom	Cat# C 1-22
FCCP	Sigma-Aldrich	Cat# C2920-10MG
SensiMix SYBR no Rox	BioLine	Cat# QT650-20
DMEM	Sigma-Aldrich	Cat# D5796
Fetal bovine serum (FBS)	Biochrom	Cat# S0615
TRISure	Bioline	Cat# BIO-38033
GW9508	Tocris	Cat# 2649
BAY-X-1005	Tocris	Cat# 3541
ethyl-3,4-dihydroxybenzoate	Biomol	Cat# LKT-P7060.5
WIN 18,446	Biomol	Cat# Cay14018-50
GIP human	Bachem	Cat# H-7586
371725,GPR43 (FFA2) Agonist	Millipore	Cat# 371725-10MG
Lactate	Sigma-Aldrich	Cat# 71718-10G
Ivabradine	Biomol	Cat# Cay15868-10
Bexarotene	Biomol	Cat# Cay11571-5
SuperScript II Reverse Transcriptase	Thermo Fisher Scientific	Cat# 18064014
Exonuclease I	New England BioLabs	Cat# M0293S
Critical Commercial Assays		
SV Total RNA Isolation System	Promega	Cat# Z3105
Pierce BCA Protein Assay Kit	Pierce	Cat# PI-23225
SensiFast cDNA Synthesis Kit	BioLine	Cat# BIO-65054
SensiMix Sybr no Rox	BioLine	Cat# QT650-20
Dual luciferase reporter assay	Promega	Cat# E1960
DNA Clean and Concentrator kit	Zymo Research	Cat# D4014
Seahorse XF96 fluxPak	Seahorse Bioscience	Cat# 102310-001
TruSeq RNA Sample Preparation Kit v2	Illumina	Cat# RS-122-2001
TruSeq Stranded mRNA Library Prep Kit	Illumina	Cat# RS-122-2101
TruSeq SBS KIT v3 - HS (50 cycles)	Illumina	Cat# FC-401-3002
Mid Output v2 kit (150 cycles)	Illumina	Cat# FC-404-2001
High Output v2 kit (75 cycles)	Illumina	Cat# FC-404-2005

(*Continued on next page*)

Continued

REAGENT or RESOURCE	SOURCE	IDENTIFIER
High Sensitivity NGS Fragment Analysis Kit	Advanced Analytical	Cat# DNF-474
Qubit dsDNA HS Assay Kit	Invitrogen	Cat# Q32851
Lipofectamine RNAi MAX	Thermo Fisher	Cat# 13778150
AMPure XP magnetic beads	Beckman Coulter	Cat# A63881
Deposited Data		
RNA-seq of mouse subcutaneous SVF cells before and after differentiation with a brown fat differentiation cocktail	This paper	ArrayExpress: E-MTAB-8344
3′ RNA-seq of differentiating (brown) mouse subcutaneous SVF cells upon knockdown of Zfp521, Fhl1, or Mxd1	This paper	ArrayExpress: E-MTAB-8343
Experimental Models: Cell Lines		
Primary murine inguinal white cells	This paper	N/A
Experimental Models: Organisms/Strains		
Mouse: C57BL/6J	Jackson Laboratory	JAX Stock No:000664
Mouse: 129S6/SvEVTac	Taconic Biosciences	129SVE
Mouse: A/J	Jackson Laboratory	JAX Stock No: 000646
Mouse: AKR/J	Jackson Laboratory	JAX Stock No: 000648
Mouse: SWR/J	Jackson Laboratory	JAX Stock No: 000689
Mouse: C57BL/6J ♂ X 129S6/SvEVTac♀	This paper	N/A
Mouse: 129S6/SvEVTac ♂ X C57BL/6J ♀	This paper	N/A
Mouse: BXD recombinant inbred strains	Andreux et al., 2012	N/A
Mouse: UCP1-Reporter mice	Wang et al., 2019	N/A
Oligonucleotides		
siRNAs used in knockdown experiments, see Table S11	This paper	N/A
Primers for qPCR, see Method Details	This paper	N/A
Software and Algorithms		
GraphPad Prism 6	Graphpad Software	N/A
Genomatix Software Suite	Genomatix AG	N/A
R	https://www.r-project.org	N/A
Fiji-ImageJ	https://imagej.net/Fiji	N/A
Other		
XF96 Extracellular Flux Analyzer	Seahorse Bioscience	N/A
FB12 Single Tube Luminometer	Titertek-Berthold	N/A
Lightcycler II	Roche	N/A

LEAD CONTACT AND MATERIALS AVAILABILITY

Further information and requests for resources and reagents should be directed to and will be fulfilled by Martin Klingenspor (mk@tum.de).

This study did not generate new unique reagents.

EXPERIMENTAL MODEL AND SUBJECT DETAILS

All animal experimentation was conducted according to the German Animal Welfare. Male mice of the C57BL6/J, 129S6sv/ev, A/J, AKR/J, SWR/J and F1 intercrossed progeny derived from C57BL6/J and 129S6sv/ev crosses as well as Ucp1promoter-Luciferase-T2A-iRFP-T2A-UCP1 knock-in mouse model (UCP1-reporter mice, C57BL6/N) bred at the animal facility of Technische Universität München in Weihenstephan, aged 5 to 6 weeks, were used to prepare primary inguinal cell cultures. All mice were fed a regular chow diet (V1124-3 M-Z; ssniff Spezialdiäten GmbH, Germany) *ad libitum* and kept at a room temperature of 23°C ± 1°C with a humidity of 55% and a 12 h light/dark cycle.

METHOD DETAILS

Primary Cell Isolation and Culture

Primary inguinal adipocytes were isolated, cultured, and differentiated from the stromal vascular fraction of inguinal fat pads as previously described (Li et al., 2014a). Isolated stromal vascular fraction cells (SVFs) were proliferated in growth medium (high-glucose DMEM containing 20% fetal bovine serum and 1% antibiotics (2:2:1) (Gentamycin, Penicillin/Streptomycin and Fungizone). Undifferentiated SVFs were harvested upon reaching sub-confluence. After reaching confluency, induction medium containing 10% fetal bovine serum (FBS), 0.5 mM isobutylmethylxanthine, 125 μM indomethacin, 1 μM dexamethasone, 850 nM insulin, 1 nM triiodothyronine (T3), 1 μM rosiglitazone was added. After 2 days of induction, cells were maintained in differentiation media (10% FBS, 850 nM insulin, 1 nM T3 and with or without 1 μM rosiglitazone). Media was changed every two days. Differentiated adipocytes were harvested after 7 days of differentiation.

siRNA Reverse Transfection

siRNA transfection of differentiating adipocytes was performed as previously established (Li et al., 2017b). Briefly, after induction, cells were reverse transfected in 12-well cell culture, 24-well cell culture or XF96 Seahorse plates using a final concentration of 50nM siRNA and 2.5 μl/ml Lipofectamine RNAiMAX (Life Technologies) in antibiotic free differentiation medium. Transfected cells were used for analyses 3 days later. We focused primarily on TFs and also more on positive regulators, as they span a range of expression levels across *in vitro* samples and also *in vivo* data. For further candidates validation, independent Dicer-substrate RNAs (DsiRNA (IDT)) were used to minimize off-target effects.

Luciferase Assay

Ucp1-driven luciferase activity was quantified using Luciferase Assay System Freezer Pack kit (E4030, Promega). Briefly, cells were lysed in 1x reporter lysis buffer by shaking for 20 min at room temperature. 10 μL cell lysate was mixed with 50 μL luciferase assay substrate solution, and bioluminescence was quantified in FB12 Single Tube Luminometer (Titertek-Berthold) (Delay time: 5 s; Measure time: 10 s).

RNA Isolation and Real-Time Quantitative PCR (qPCR)

Total RNA was isolated with TRIsure (Bioline) and purified using columns from SV Total RNA Isolation System Kit (Promega) according to the manufacturer's instructions. 500ng RNA was subjected to cDNA synthesis using SensiFAST cDNA Synthesis Kit (Bioline). qPCR was performed in 384 well plates (4titude) using Lightcycler 480 II (Roche). The RNA abundance of each gene was normalized to housekeeping gene TFIIB. The following primers were used:

Ucp1 F: 5′-GTACACCAAGGAAGGACCGA-3′, R: 5′-TTTATTCGTGGTCTCCCAGC-3′;
Tfiib F: 5′-TGGAGATTTGTCCACCATGA-3′, R: 5′-GAATTGCCAAACTCATCAAAACT-3′;
Fhl1 F: 5′-GTGAGCCACCCAGTCTCTAA-3′, R: 5′- AGTAGTCGTGCCAGGATTGT −3′;
Mxd1 F: 5′-GCCTGTGCCTAGAGAAGCTA-3′, R: 5′-GCTGTCCATCCGAGTCCTC-3′;
Zfp521 F: 5′-AGTGTCACCTGATAGAGCACA −3′, R: 5′-ACTTCTGTGGGCATTGTGTG-3′;

RNA-Seq and Analysis

RNA integrity of all samples used for sequencing was assessed using an RNA 6000 Nano chip (Agilent, Santa Clara, CA, USA).

For standard TruSeq (primary cultured adipocytes derived from five inbred mouse strains), RNA-seq libraries were prepared using the TruSeq RNA Sample Prep kit v2, pooled in to 7 libraries per lane and sequenced in 50 nt single-end (plus barcode) format, using the TruSeq SBS kit v3-HS, to reach a depth of at least 25 million read pairs per sample on the Illumina HiSeq 2000 platform (Illumina, San Diego, CA, USA) at the Fritz Lipman Institute for Aging Research (Jena, Germany). To generate RNA-seq data for the allelic imbalance analysis, TruSeq libraries were prepared using the TruSeq Stranded mRNA Library Prep Kit (Illumina,#RS-122-2101) and following the manufacturer's instructions. Libraries were paired-end sequenced (75 nt each) with the NextSeq 500 using the Mid Output v2 kit (150 cycles) (Illumina, #FC-404-2001) at the EPFL Gene expression core facility (Switzerland).

For barcoded mRNA sequencing, RNA sequencing libraries were prepared following the BRB-seq protocol (Alpern et al., 2019). Briefly, each RNA sample was reverse transcribed in a 96-well plate using SuperScriptTM II Reverse Transcriptase (Lifetech 18064014) with individual barcoded oligo-dT primers. Next, all the samples were pooled together, purified using the DNA Clean and Concentrator kit (Zymo Research #D4014), and treated with exonuclease I (NEB or New England BioLabs #M0293S). Double-stranded cDNA was generated by the second stand synthesis via the nick translation method (Alpern et al., 2019). Full-length double-stranded cDNA was purified with 30 μL (0.6x) of AMPure XP magnetic beads (Beckman Coulter, #A63881) and eluted in 20 μL of water. The Illumina compatible libraries were prepared by tagmentation of 5 ng of full-length double-stranded cDNA with 1 μL of in-house produced Tn5 enzyme (11 μM). The final library was amplified using 15 cycles and the fragments ranging 200–1000 bp were size-selected using AMPure beads (Beckman Coulter, #A63881) (first round 0.5x beads, second 0.7x). The libraries were profiled with the High Sensitivity NGS Fragment Analysis Kit (Advanced Analytical, #DNF-474) and measured with the Qubit dsDNA HS Assay Kit (Invitrogen, #Q32851) prior to pooling and sequencing using the Illumina NextSeq 500 platform using a custom primer and the High Output v2 kit (75 cycles) (Illumina, #FC-404-2005).

For transcriptomics-related analyses, fastq files containing single-end sequenced tags (reads) from three replicate experiments each were analyzed. Reads from each sample were trimmed and filtered using prinseq 0.20.3 (Schmieder and Edwards, 2011) with the parameters "-custom_params 'A 70%;T 70%;G 70%;C 70%' -trim_tail_left 36 -trim_tail_right 36 -lc_method dust -lc_threshold

45 -min_gc 1 -out_format 3" and cutadapt 1.5 (Martin, 2011) with the parameters "-m 36 -q 20." The retained tags were aligned to the Ensembl 75 (Zerbino et al., 2018) gene annotation of the NCBI38/mm10 mouse genome using Bowtie 0.12.9 and the parameters "-a–best–strata -S -m 100." Expression levels per transcript and gene were estimated using mmseq-1.0.8 (Turro et al., 2011) with default parameters. Quantile normalized expression estimates were transformed into pseudo-counts by un-logging, un-standardizing and multiplying with gene length. Pseudo-counts were then normalized using mean-variance modeling at the observational level, as implemented in the voom() function in limma_3.30.4 (Ritchie et al., 2015). Differential expression was computed on the normalized values using the limma_3.30.4 pipeline at an FDR of 0.01 and fold-change cutoff of 2 (|FC|). Heatmaps displaying (row-normalized by z-score transformation) log2 expression values were generated using the function heatmap.2() in gplots_3.0.1. Medians of the normalized expression values (log2, before the z-score transformation) are displayed as an additional sidebar left of the respective heatmaps.

For the data from barcoded mRNA sequencing (KD experiments presented in Figures 5 and S5), fastq files containing 62 bp long single-end sequenced tags (reads) from at least 3 (Zfp521 KD) and 4 (Mxd1 and Fhl1 KD) biological replicates were trimmed and filtered using prinseq 0.20.3 with the parameters "-custom_params 'A 70%;T 70%;G 70%;C 70%' -trim_tail_left 36 -trim_tail_right 36 -lc_method dust -lc_threshold 45 -min_gc 1 -out_format 3" and cutadapt 1.5 with the parameters "-m 36 -q 20" and the Nextera adaptor sequence. The retained tags were evaluated using FastQC v0.11.2 and aligned to the Ensembl 84 gene annotation of the NCBI38/mm10 mouse genome using STAR 2.4.0g (Dobin et al., 2013) with the parameters "–runThreadN 4–runMode alignReads–outFilterType BySJout–outFilterMultimapNmax 20–alignSJoverhangMin 8 –alignSJDB overhangMin 1–outFilterMismatchNmax 999–outFilterMismatchNoverLmax 0.04–alignIntronMin 20–alignIntronMax 1000000–alignMatesGapMax 1000000 g–outSAMtype BAM SortedByCoordinate." Number of tags per gene were calculated using htseq-count 0.6.0 33 with the parameters "htseq-count -m intersection-nonempty -s no -a 10 -t exon -i gene_id." Raw counts were normalized using mean-variance modeling at the observational level, as implemented in the voom() function in limma_3.30.4. DE was computed on the normalized values using the limma_3.30.4 pipeline at an FDR of 0.1 (or 0.3) and FC cutoff of 2.

Allelic Imbalance Analysis

The analysis of the F1 hybrids was performed as previously described (Shen et al., 2014). In brief, reads were aligned with Bowtie v0.12.9 to a hybrid reference transcriptome. The reference transcriptomes were based on the Ensembl Release 70 cDNA files and the Wellcome Trust Mouse Genomes Project Release 2 VCF files. The 129S1 reference was used for the 129S6 strain. Only autosomal genes with known exonic polymorphisms between 129S and BL/6J were included in this analysis. mmseq-1.0.8 was used to estimate gene expression levels and mmdiff (Turro et al., 2014) to determine imprinted genes, as well as the primary gene regulatory mode (*cis*, trans or *cis* and trans). First, a null model (no imprinting) that assumes allelic expression differences are the same in B6x129S6 and 129S6xB6 was compared to an imprinting model, which assumes that allelic expression differences have a similar magnitude but opposite signs in B6x129S6 as in 129S6xB6. Next, a comparison of four models (conserved, *cis*, trans, *cis* and trans) was performed using mmdiff after filtering out genes putatively imprinted. While the conserved model assumes no DE between the F0's and no allelic expression imbalance (AEI) in the F1s, the *cis* model assumes there is DE between the F0's that is equal to the AEI in the F1's. The trans model assumes there is DE between the F0's but no AEI in the F1's. The *cis* and trans model assumes that there is DE in the F0's, but it is unequal to the AEI in the F1's. In the reported classification, the winning model must have a posterior probability >0.5, and the posterior probability of the winning model must be at least twice that of the second-best model, assuming an equal prior probability of 0.25 for each of the four models. Finally, we calculated the weighted log fold change for each gene as previously described (Turro et al., 2014).

Network Analysis

Network analysis was performed as recently described, using the R package SCENIC 1.0.0-0.2 (Aibar et al., 2017). In brief, we first derived a gene co-expression network based on all RNA-seq data using GENIE 1.2.1. Next, we identified so-called "regulons" – groups of genes regulated by one particular TF as predicted based on DNA-binding motifs, using the integrated annotation mm9_direct_motifAnnotation and a set of 1,620 TFs (Table S10). Finally, we estimated activity levels for each TF based on its expression level as well as that of its regulon, as previously described (Aibar et al., 2017). We displayed the obtained regulatory relations using igraph 1.2.2 and an initial cutoff of 0.003. In the network displayed in Figure 5F, each link is determined by the expression correlation, and connections supported by regulatory information (motif presence) are in black rather than gray, highlighting most likely direct regulators. Only a core subset of TFs of interest are displayed as nodes, including (1) known core (brown) adipogenesis regulators, (2) briteDECoG.F1s.UP predicted to directly regulate Ucp1 expression (Figures 3J and S5G) and (3) validated regulators (Figure 4D). Node sizes correspond to linkage degree (number of connections going in/out), and the color to change in expression upon differentiation of 129S6 cells. Second, we displayed a network consisting of all direct regulatory connections among all active TFs as well as Ucp1 and the validated TFs Fhl1 and Zfp521, which had no assigned regulon (Figures 5G–5I). Here, we included as nodes all TFs showing a change in activity either across differentiation or across KDs and the links represent predicted regulatory relations.

Western Blot Analysis

For immunological detection, protein lysates (30μg) were resolved by electrophoresis in 12.5% SDS-PAGE gel, electroblotted onto a PVDF membrane (Millipore) by using a Trans-Blot SD. Semi-Dry Transfer Cell (Bio-Rad) and probed with either rabbit anti-UCP1 antibody (1:10000) or mouse anti-ACTIN antibody (1:10000). Secondary antibodies conjugated to IRDye 680 or IRDye 800 (Li-Cor Biosciences) were incubated at a dilution of 1:20000. Fluorescent images were captured by an Odyssey fluorescent imager (Li-Cor Biosciences). Images were further processed with Fiji-ImageJ.

Respirometry

Oxygen consumption rate (OCR) was measured at 37°C using an XF96 extracellular flux analyzer as described previously (Li et al., 2014b, 2017b). To avoid unspecific uncoupling caused by an excessive rise of intracellular free fatty acids levels released during lipolysis, 2% essentially fatty acid free bovine serum albumin (BSA) was included in the unbuffered respiration medium (DMEM basal medium (Sigma D) supplemented with 25 mM glucose, 31 mM NaCl, 2 mM GlutaMax and 15 mg/l phenol red, pH 7.4). The 10X drug solutions were prepared in respiration medium without BSA. The rate of O2 consumption (OCR) was determined by 3 or 5 cycles of: 2 min mix, 2 min wait and 3 min measurement.

QUANTIFICATION AND STATISTICAL ANALYSIS

All computational analyses were performed using R version 3.3.2 and Bioconductor version 3.4. All t tests were unpaired if not otherwise specified. The Gene Ontology enrichment analysis was performed using the topGO 2.26.0 package, the ''elimCount'' method and a p value cutoff of 0.001.

Significant differences were assessed by two-tailed Student's t test for single comparisons or Two-way ANOVA when two or more groups were compared (Prism 6.0 software). A p value < 0.05 was considered a statistically significant difference. $^{*}p < 0.05$, $^{**}p < 0.01$, $^{***}p < 0.001$.

DATA AND CODE AVAILABILITY

The accession number for the RNA-seq data presented in this article is ArrayExpress (https://www.ebi.ac.uk/arrayexpress/): E-MTAB-8343 and E-MTAB-8344.